Check for updates

ADVANCING EARTH AND SPACE SCIENCES

JGR Solid Earth

RESEARCH ARTICLE

10.1029/2025JB032879

Stress Barriers and Their Impact on Rupture Propagation

F. Paglialunga[1], J. P. Ampuero[1], and F. Passelègue[1]

[1]Université Côte d'Azur, Observatoire de la Côte d'Azur, IRD, CNRS, Géoazur, Sophia Antipolis, France

Key Points:

- Lab experiments demonstrate that stress heterogeneity strongly influences rupture dynamics, often leading to delayed triggering phenomena
- Five rupture–barrier interaction mechanisms identified: arrest and deceleration, static and dynamic triggering, barrier-induced supershear transition
- The specific interaction mechanism depends on the relative strength of the stress heterogeneity along the fault

Supporting Information:

Supporting Information may be found in the online version of this article.

Correspondence to:

F. Paglialunga,
federica.paglialunga@geoazur.unice.fr

Citation:

Paglialunga, F., Ampuero, J. P., & Passelègue, F. (2026). Stress barriers and their impact on rupture propagation. *Journal of Geophysical Research: Solid Earth*, *131*, e2025JB032879. https://doi.org/10.1029/2025JB032879

Received 29 AUG 2025
Accepted 19 DEC 2025

Author Contributions:

Conceptualization: F. Paglialunga, J. P. Ampuero, F. Passelègue
Data curation: F. Paglialunga
Formal analysis: F. Paglialunga
Funding acquisition: F. Paglialunga, F. Passelègue
Investigation: F. Paglialunga
Project administration: J. P. Ampuero
Resources: F. Passelègue
Supervision: J. P. Ampuero
Validation: F. Paglialunga
Visualization: F. Paglialunga
Writing – original draft: F. Paglialunga
Writing – review & editing: J. P. Ampuero, F. Passelègue

© 2026. The Author(s).
This is an open access article under the terms of the Creative Commons Attribution License, which permits use, distribution and reproduction in any medium, provided the original work is properly cited.

Abstract Earthquake ruptures often exhibit complex behaviors, including abrupt arrest followed by delayed re-nucleation. While on-fault stress heterogeneity is a recognized contributing factor, as it can arrest or slow down rupture propagation, its interaction with propagating ruptures remains complex and not fully understood. Here, we study frictional ruptures under controlled laboratory conditions by imposing a heterogeneous stress field along an artificial fault. This setup consistently led to the spontaneous emergence of a well-defined stress barrier. Our results show that the presence and strength of the stress barrier systematically influence rupture propagation, sometimes in non-trivial ways. As expected, strong barriers tend to arrest ruptures, while weaker ones reduce their velocity, inducing a time delay in the rupture propagation. However, we also observe several less-intuitive outcomes, including static triggering, barrier-induced supershear transition, and dynamic triggering. We elucidate the physics behind each interaction mechanism through Linear Elastic Fracture Mechanics (for the arrest and deceleration mechanisms) and the Rate-and-State framework (for the static triggering). Interestingly, static triggering and barrier-induced supershear transitions can enable rupture propagation beyond barriers that are expected to arrest ruptures. Similarly, dynamic triggering can accelerate the onset of rupture beyond barriers that decelerate ruptures. Moreover, our experiments show that the barrier efficiency evolves over successive earthquake cycles, weakening with repeated partial ruptures and becoming permanent once complete ruptures break through the fault. This experimental study underscores the critical role of stress heterogeneity in controlling the dynamics of frictional ruptures and offers new insights into the physics of delayed rupture triggering.

Plain Language Summary Earthquakes do not always break steadily through a fault. They can stop abruptly and restart later on, or be unexpectedly triggered. Many factors could cause this behavior, but the stress acting on the fault is surely one of the most important. This stress is often heterogeneous and can control the way the rupture propagates and stops. To investigate this, we conducted laboratory experiments on an artificial fault, applying an uneven shear stress that led to the spontaneous formation of a stress barrier. When this barrier was strong, it stopped the ruptures, while when it was weaker, it slowed them down. Surprisingly, we also observed cases where the barrier caused ruptures to restart after a small delay, switch to faster modes of rupture, or trigger new ruptures beyond the barrier. Moreover, over repeated earthquake cycles, the barrier evolved: partial ruptures weakened it until a full rupture broke through and made it permanent. We also gained basic insights into these processes from theoretical models. These results demonstrate that stress barriers play a crucial role in how earthquakes start, stop, and sometimes restart. Understanding this behavior can help explain puzzling earthquake observations in nature, such as delayed triggering and sudden changes in rupture speed.

1. Introduction

Earthquake rupture propagation is fueled by the energy stored in the medium surrounding the causative fault. As long as this available energy remains sufficient to overcome energy dissipation, the rupture will continue to advance. However, obstacles along the fault can impede this progression, potentially altering or stopping the rupture, depending on their strength. These obstacles can arise from various sources, including geometrical complexities such as fault bends (Dal Zilio et al., 2019; Gabrieli & Tal, 2025; Rodriguez Padilla et al., 2024) or segmented fault structures (Romanet et al., 2018), frictional heterogeneities such as velocity-strengthening patches (Dublanchet et al., 2013; Kaneko et al., 2010; Lapusta & Rice, 2003; Molina-Ormazabal et al., 2023; Noël et al., 2025; Song & McLaskey, 2024; L. Wang et al., 2024), and heterogeneities of on-fault initial stresses. Among the earliest numerical studies of dynamic rupture, Das and Aki (1977) investigated the effect of stress barriers on propagating ruptures and their associated slip distributions. Subsequent work by Day (1982); Das and Kostrov (1983), Fukuyama and Madariaga (2000) studied the response of a dynamically propagating rupture to either single asperities and increasingly complex heterogeneous distributions, revealing important implications

for rupture velocity. Later, Ripperger et al. (2007) explored the role of heterogeneous stress distribution with varying statistical properties, highlighting its influence on rupture size and seismic observables. Using 3D modeling, Dunham et al. (2003) demonstrated that a stress barrier can not only alter the rupture dynamics but also trigger a transition to supershear velocity. Similarly, Lapusta and Liu (2009) showed that normal stress heterogeneity can affect both rupture dynamics and the long-term evolution of fault activity over several seismic cycles.

Recent laboratory studies have further illustrated the influence of heterogeneous stress distribution on frictional rupture behavior. One end-member scenario is rupture arrest caused by stress heterogeneity, in particular a low shear stress area acting as a barrier to rupture propagation (Bayart et al., 2016, 2018; Ke et al., 2018). Other studies have explored the influence of a reduction of local effective stress due to either fluid injection (S. B. Cebry, Ke, & McLaskey, 2022) or a simulated one (Fryer et al., 2024), showing that different rupture sizes can be obtained depending on the stressing conditions. Buijze et al. (2020), S. B. Cebry, Ke, Shreedharan, et al. (2022), Paglialunga, Passelègue, et al. (2025) showed that stress heterogeneity along the fault that emerges spontaneously from the loading boundary conditions has an impact on the location of rupture nucleation and the complexity of the seismic sequences. Moreover, S. B. Cebry et al. (2023) showed that a highly localized normal stress bump can act either as a barrier (hindering rupture propagation) or as an asperity (easing rupture propagation), strongly influencing rupture propagation and wave radiation (S. Cebry & McLaskey, 2024).

The ability of a frictional rupture to overcome a stress barrier can be interpreted energetically within the framework of Linear Elastic Fracture Mechanics (LEFM) for shear cracks (Kammer et al., 2015; Svetlizky & Fineberg, 2014). An advancing rupture produces a dynamic energy release rate at its tip (G), and rupture arrest is controlled by the static energy release rate G_0. For propagation to be sustained, G_0 must be equal to or exceed the fracture energy opposing the rupture (G_c). When $G_0 < G_c$, the rupture arrests. This condition can arise from a locally elevated G_c, associated with a high-strength barrier, or from a locally reduced G_0, often linked to a low-stress barrier (Madariaga & Olsen, 2001), or from the combined effect of both factors. Laboratory experiments have shown that a sufficiently high G_c barrier can indeed arrest rupture propagation (Gvirtzman & Fineberg, 2021, 2023; Morad et al., 2025). Remarkably, these studies also reported that ruptures frequently re-nucleate on the opposite side of the barrier after a certain time delay. Similar delayed re-nucleation behavior was observed in S. B. Cebry et al. (2023); Paglialunga, Passelègue, et al. (2025). However, the underlying physical mechanisms responsible for this time delay remain poorly constrained and are the subject of ongoing investigation.

The concept of a propagating rupture decelerating or arresting, then re-accelerating or re-nucleating after a certain period, is known as delayed triggering (Freed, 2005). This term encompasses a range of phenomena, including viscoelastic relaxation, poroelastic rebound, and afterslip, that can redistribute stresses between faults over timescales from minutes to decades. Stress changes can be static, such as those produced by the arrest of a rupture (J.-C. Wang et al., 2003; Sheng et al., 2024). They can also be dynamic, such as transient stress perturbations resulting from seismic waves radiated by ruptures on adjacent fault segments or neighboring faults (Brodsky et al., 2000; Gomberg et al., 2003; Gomberg & Johnson, 2005; Hill et al., 1993). These mechanisms give rise to static and dynamic triggering, respectively.

Several natural earthquakes have exhibited such delayed triggering behavior during their complex rupture. For instance, during the 2007 M_w 8.0 Pisco earthquake, two major asperities separated by about 60 km failed sequentially with a temporal gap of approximately 60 s (Sladen et al., 2010). Similarly, the 2024 M_w 7.5 Noto earthquake involved the rupture of two distinct patches separated by a 10 s delay (Xu et al., 2024). Smaller repeating earthquakes along the San Andreas fault were found to be associated with triggering phenomena induced by postseismic slip (Lui & Lapusta, 2016). Understanding the physical mechanisms underpinning such triggering phenomena is critical for improving earthquake forecasting, including the integration of physics-based constraints into aftershock prediction models (Hardebeck et al., 2024).

In this study, we focus on one source of delayed triggering, stress, experimentally investigating the interaction between propagating frictional ruptures and stress heterogeneity. We identify a continuum of behaviors ranging from expected rupture arrest to more complex responses such as static and dynamic triggering. The governing physics of each interaction mechanism is examined, using the theoretical framework of linear elastic fracture mechanics and the slip-rate and state-dependent friction law.

21699356, 2026, 2, Downloaded from https://agupubs.onlinelibrary.wiley.com/doi/10.1029/2025JB032879 by Charles University T.G., Wiley Online Library on [19/02/2026]. See the Terms and Conditions (https://onlinelibrary.wiley.com/terms-and-conditions) on Wiley Online Library for rules of use; OA articles are governed by the applicable Creative Commons License

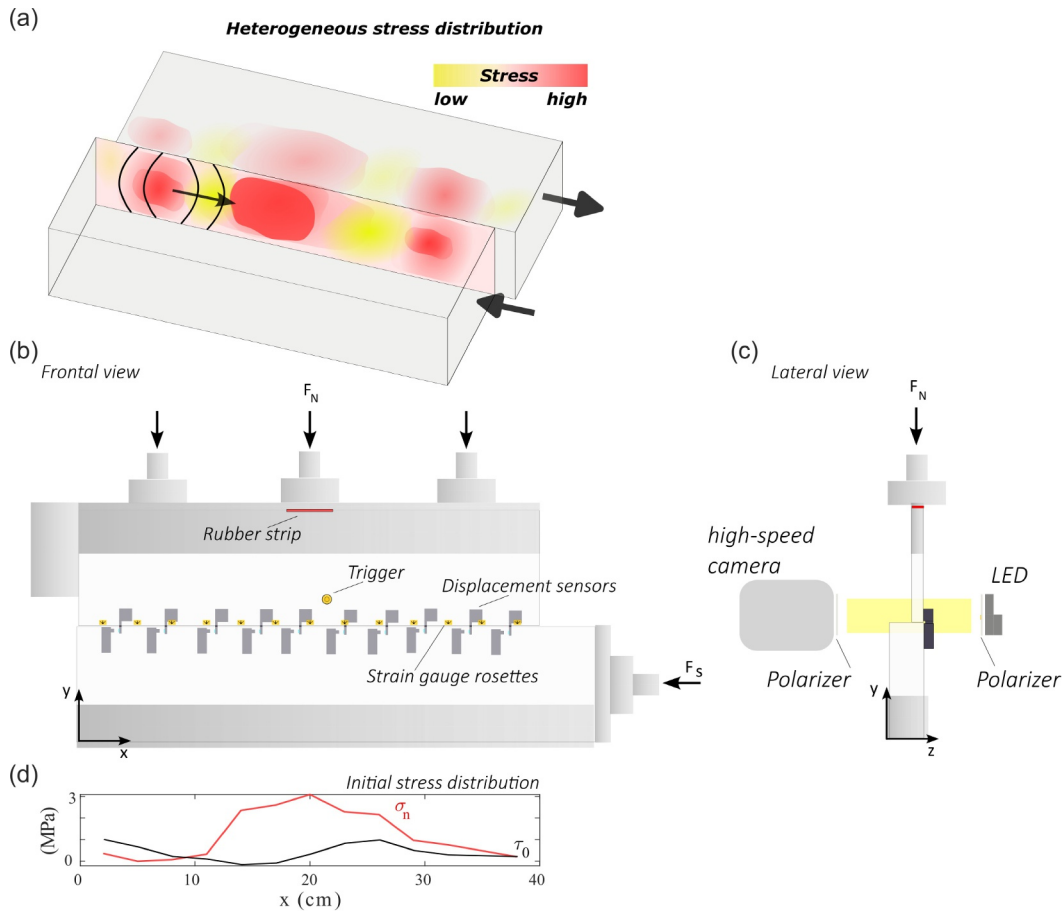

Figure 1. Experimental apparatus located at ESEILA in Geoazur, Université Côte d'Azur. (a) Sketch of the laboratory fault system, subjected to heterogeneous stress conditions. (b) Frontal view. Two PMMA samples are positioned one on top of the other to generate a 40 × 1 cm bare interface. Thirteen strain gauge rosettes and ten displacement sensors are positioned at equidistant locations along the fault. A piezoelectric sensor glued in the middle of the fault acts as a trigger to activate camera recording. A rubber strip located below the central piston modifies the externally applied stress. (c) Lateral view reveals the presence of a high-speed camera positioned exactly in front of the artificial fault. On the opposite side, a white light is emitted and polarized for the first time. After being transmitted through the sample, it is polarized once again (perpendicularly to the direction of the first polarization), before reaching the camera lens. (d) Normal and shear stress distribution at the beginning of a representative experiment.

2. Methods

Frictional rupture experiments were performed using a direct shear biaxial apparatus (Figure 1) (Fryer et al., 2024). The experimental setup consists of two cuboids pressed together through three vertical pistons applying a normal load, and later sheared by a horizontal piston applying the shear load. The two samples have the following dimensions: 40 × 10 × 1 cm for the top block and 45 × 10 × 3 cm for the bottom block, in contact along an artificial fault of 40 × 1 cm. The analog material used was poly (methyl methacrylate) (PMMA) characterized by elastic properties $E_{\text{stat}} = 3.5$ GPa and $\nu = 0.33$, and seismic velocities $C_p = 2700$ m/s, $C_s = 1350$ m/s and $C_r = 1250$ m/s.

The fault was equipped with thirteen strain gauge rosettes (i.e., assembly of three strain gauges oriented at 45°, 90°, and 135° relative to the fault direction), equally spaced and located around 3 mm from the fault plane. The measured strain tensors were converted to stress assuming plane stress conditions. Ten displacement sensors were also positioned at equidistant locations along the fault, 1 mm away from the fault plane. Each displacement sensor location is characterized by one fiber-optic sensor glued to the bottom sample and a target mirror glued to the top sample to measure relative displacement (Figure 1). Both strain and displacement measurements were acquired at a frequency of 2 MHz.

21699356, 2026, 2, Downloaded from https://agupubs.onlinelibrary.wiley.com/doi/10.1029/2025JB032879 by Charles University T.G., Wiley Online Library on [19/02/2026]. See the Terms and Conditions (https://onlinelibrary.wiley.com/terms-and-conditions) on Wiley Online Library for rules of use; OA articles are governed by the applicable Creative Commons License

21699356, 2026, 2, Downloaded from https://agupubs.onlinelibrary.wiley.com/doi/10.1029/2025JB032879 by Charles University T.G., Wiley Online Library on [19/02/2026]. See the Terms and Conditions (https://onlinelibrary.wiley.com/terms-and-conditions) on Wiley Online Library for rules of use; OA articles are governed by the applicable Creative Commons License

Dynamic rupture evolution was captured using a high-speed camera operating at 1 million frames per second. The camera was triggered by acoustic waves radiated from the rupture and detected by a piezoelectric sensor located at the center of the top block, approximately 3 cm away from the fault, with a triggering threshold of 80 mV. Stress variations were further monitored via photoelasticity, exploiting the stress-induced birefringence of PMMA (Fryer et al., 2024; Gounon et al., 2022; Guérin-Marthe et al., 2019; Latour et al., 2013, 2024; Nielsen et al., 2010; Paglialunga et al., 2023; Schubnel et al., 2011; Xia et al., 2004). A light source (LED) is placed on the opposite side of the experimental fault and polarized for the first time. Once the light traverses the stressed sample, it is split into different beams whose propagation velocity is modified by the stress in the sample. The emitted light is finally polarized once again (cross polarization) before being acquired by the camera. This creates dark and light fringes indicating the principal stress orientation. Changes in light intensity were then used to track rupture propagation during each event. Specifically, a line 0.06 mm from the fault was extracted from each frame to generate videograms, providing spatio-temporal maps of light intensity and thus a direct record of rupture front dynamics (Figure S1 in Supporting Information S1).

A uniform normal stress, applied through three hydraulic pistons, was maintained between 100 and 200 bars (as measured at the pump). Shear loading was imposed under flow-control conditions at a rate of 0.5 cm^3/min. To introduce a controlled stress heterogeneity, a 4 cm-long rubber strip was inserted between the top sample and the steel distribution plate at the center of the fault. Despite its modest thickness of only 2 mm, the strip effectively concentrated normal stress in that region, thereby modifying the on-fault stress distribution (Figures 1d and 2a–2e).

This study used five experiments, each providing an average of 15 events, resulting in 75 analyzed events overall.

3. Results

Each experiment began with a sequence of partial rupture events, which progressively transitioned into complete ruptures that occurred until the end of the experiment. The occurrence of each rupture modified the on-fault shear stress distribution $\tau(x)$, thereby influencing the behavior of subsequent events (Figures 2b–2e).

3.1. Seismic Sequence

A representative experiment is shown in Figure 2. The fault hosted sixteen events, of which the first eight were partial (i.e., the rupture extension was contained within the fault length), and the remaining eight were complete (i.e., the rupture propagated along the whole fault length). The on-fault stress distribution evolved during the experiment. During the first phase, characterized by partial ruptures (dashed lines in Figures 2b–2e), the normal stress in the central part of the fault decreased from 2.8 MPa to around 1.8 MPa (Figure 2b). Conversely, the shear stress increased in the region $x = 10 - 20$ cm due to the arrest of the repeated partial ruptures (Figures 2c and 2d). This coincides with a region of negative potential stress drop characterizing partial ruptures (dashed lines in Figure 2e). The stress drop was calculated as $\Delta\tau(x) = \tau_0(x) - \tau_{res}(x)$, with τ_{res} the residual stress defined as the final stress for the first observed complete rupture, assuming it comparable for all complete ruptures (solid lines in Figure 2d). On the contrary, during the second phase, characterized by complete ruptures (solid lines in Figures 2b–2e), the normal as well as the initial and final shear stress profiles remained largely unchanged (solid lines in Figures 2b–2d), and the measured stress drop was consistently positive (solid lines in Figure 2e).

Each rupture event was captured in a videogram, which was used to analyze the history of the rupture propagation front. In the first event, the rupture nucleated at the left edge of the fault, propagated over a distance of 10 cm, and subsequently arrested (Figure 2f). Several successive partial events exhibited similar behavior. For example, event 5 nucleated at $x = 5$ cm, propagated bilaterally, and arrested at $x = 12$ cm, emitting classical arrest S-waves (Figure 2g). Differently, event 6 nucleated at $x = 27$ cm, propagated bilaterally, and arrested at $x = 20$ cm (Figure 2h). The arrest location is not arbitrary but coincides with the low shear stress region emerging in Figure 2c, regardless of the nucleation location. Event 9 is the first complete event occurring in the sequence. The rupture nucleated at $x = 5$ cm and propagated bilaterally. After a first propagation phase, it decelerated significantly at $x = 16$ cm, and only after a time interval did it resume its propagation toward the opposite fault edge (Figure 2i). The following ruptures (f.e., events 10 and 16) showed a similar behavior, with the rupture decelerating around $x = 16$ cm before continuing their propagation (Figures 2j and 2k). However, the duration of the deceleration phase became shorter toward the end of the sequence. The deceleration phase systematically occurred at a region where the normal stress presented a local increase.

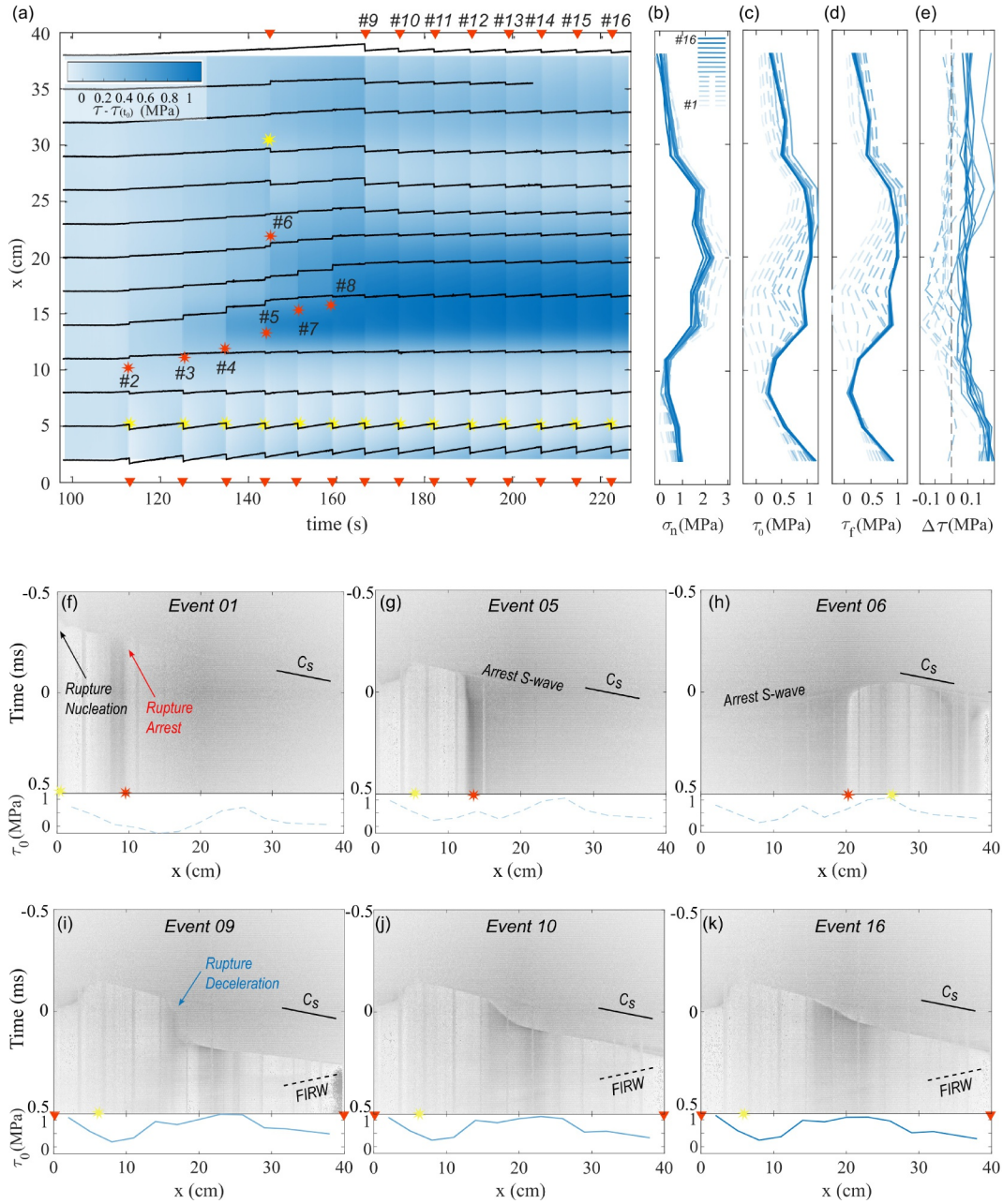

Figure 2. Results of a representative experiment (Exp 04). (a) Temporal evolution of shear stress at 13 measuring locations. The curves are offset on the *y*-axis by the measuring location. In the background, the shear stress distribution obtained by spatial interpolation of the mechanical measurements, with respect to the time $t_0 = 100$ s. For each event, a yellow star marks the nucleation location, a red star marks the arrest location, and red triangles mark ruptures that reach the free edge of the interface, as measured on the videograms. (b, c) indicate the background normal and shear stress spatial distribution before each rupture, (d) the final shear stress after each rupture, and (e) the potential stress drop ($\Delta\tau = \tau_0 - \tau_{res}$). Note that the residual stress τ_{res} is defined as the final stress (τ_f) of complete ruptures. Dashed curves refer to partial events, and solid curves to complete events. (f–m) show characteristic videograms of selected events. A panel below each subplot shows the initial shear stress before the event (similar to (c)). In particular, (f–h) show partial events, and (i–k) complete events.

21699356, 2026, 2, Downloaded from https://agupubs.onlinelibrary.wiley.com/doi/10.1029/2025JB032879 by Charles University T.G., Wiley Online Library on [19/02/2026]. See the Terms and Conditions (https://onlinelibrary.wiley.com/terms-and-conditions) on Wiley Online Library for rules of use; OA articles are governed by the applicable Creative Commons License

In the described laboratory sequence, the on-fault stress distribution dictated the nature of the single events. This first observation demonstrates that stress heterogeneity can influence rupture propagation in various ways, including arresting or delaying it.

3.2. Rupture–Barrier Interaction Mechanisms

Five distinct mechanisms were identified for the interaction between a propagating rupture and stress heterogeneity. One representative example of each mechanism is shown in Figure 3.

The first mechanism is *rupture arrest*. The partial rupture shown in Figure 3a nucleated at $x = 5$ cm, propagated bilaterally, reached a significant rupture velocity $\left(C_f \approx C_s\right)$, and arrested at $x = 14$ cm. During propagation, the fault experienced a stress drop within the ruptured area and a stress increase adjacent to the arrest location (white curves in Figure 3a). The slip evolution reveals the emergence of an initial slip patch at the nucleation point, which grew over time, reaching a final slip of 11 μm in the ruptured zone and negligible slip in the unruptured region (Figure 3c).

The second interaction mechanism is *static triggering*. This occurs when a partial rupture modifies the stress state in an adjacent region, promoting a subsequent rupture. In Figure 3d, a first rupture nucleated at $x = 6$ cm, propagated bilaterally, and halted at $x = 15$ cm. As in the rupture arrest case, the fault experienced a stress drop in the ruptured segment and a stress increase near the arrest point. After a delay of 0.9 ms, a second rupture nucleated at $x = 26$ cm and propagated bilaterally, breaking the entire fault. Notably, no rupture front propagation was observed during the time interval between the two subevents, with a propagation velocity effectively equal to zero (Figure 3e). The slip evolution confirms this behavior, showing two distinct slip patches corresponding to the two subevents and no slip associated with the delay interval (orange colorbar in Figure 3f).

The third observed mechanism is the *barrier-induced supershear transition* (Figure 3g). In this example, the rupture nucleated similarly to the previous cases but did not arrest. It decelerated at $x = 16$ cm, reaching a minimum propagation velocity of $0.1\,C_s$. This deceleration phase lasted about 0.17 ms. Immediately after, a new rupture front emerged and rapidly accelerated to a supershear velocity of $0.9\,C_p$ (Figure 3h). The slip evolution shows an initial patch forming near the nucleation point and growing as the rupture advanced, reaching a final slip of approximately 15 μm. Minimal slip is associated with the deceleration phase.

Another mechanism, often considered alongside rupture arrest, is *rupture deceleration*. In the example shown in Figure 3j, the rupture nucleated at $x = 6$ cm and propagated with a rupture velocity $C_f = 0.7\,C_s$. Upon reaching $x = 16$ cm, the rupture front smoothly decelerated to $C_f = 0.2\,C_s$ (Figure 3k). After traveling approximately 4 cm at this reduced velocity, it re-accelerated to $C_f = C_s$, maintaining that velocity until the end of propagation. The slip evolution highlights the significant contribution of the deceleration phase to the final slip distribution (Figure 3l), consistent with a rupture event exhibiting variable propagation velocity.

The final interaction mechanism is *dynamic triggering*. This behavior was observed in only one event (Figures 3m and 3n). The rupture nucleated at $x = 28$ cm, propagated bilaterally, and reached $C_f = 0.9\,C_s$. It then decelerated sharply to $C_f = 0.05\,C_s$. After a delay of 0.2 ms, the rupture abruptly accelerated and propagated toward the fault edge. This re-acceleration was not spontaneous but triggered by interface waves reflected from the right fault edge (at $x = 40$ cm). Consistent with the rupture history, the slip evolution shows an initial patch at $x = 27$ cm growing as the rupture advanced (Figure 3o). The deceleration phase (orange colorbar) began before the rupture reached the fault edge and is associated with (a) an increase in slip as the rupture front arrived at the free boundary at $x = 40$ cm (red region) and (b) an additional slip contribution generated by the leftward-propagating interface wave reflecting back toward the stress heterogeneity (lighter orange/yellow). The significant slip occurring at the right edge of the fault is typical of ruptures that reach the free surface (Huang et al., 2014).

All examined events exhibit crack-like rupture behavior, as indicated by the slip distributions (where slip continues to increase in the nucleation region) and by the photoelastic measurements, which show no evidence of healing fronts. We therefore adopt crack-like models to describe the interaction mechanisms discussed above. Note that these mechanisms could be influenced by the rupture style (i.e., pulse-like ruptures (Barras et al., 2023)).

21699356, 2026, 2, Downloaded from https://agupubs.onlinelibrary.wiley.com/doi/10.1029/2025JB032879 by Charles University T.G., Wiley Online Library on [19/02/2026]. See the Terms and Conditions (https://onlinelibrary.wiley.com/terms-and-conditions) on Wiley Online Library for rules of use; OA articles are governed by the applicable Creative Commons License

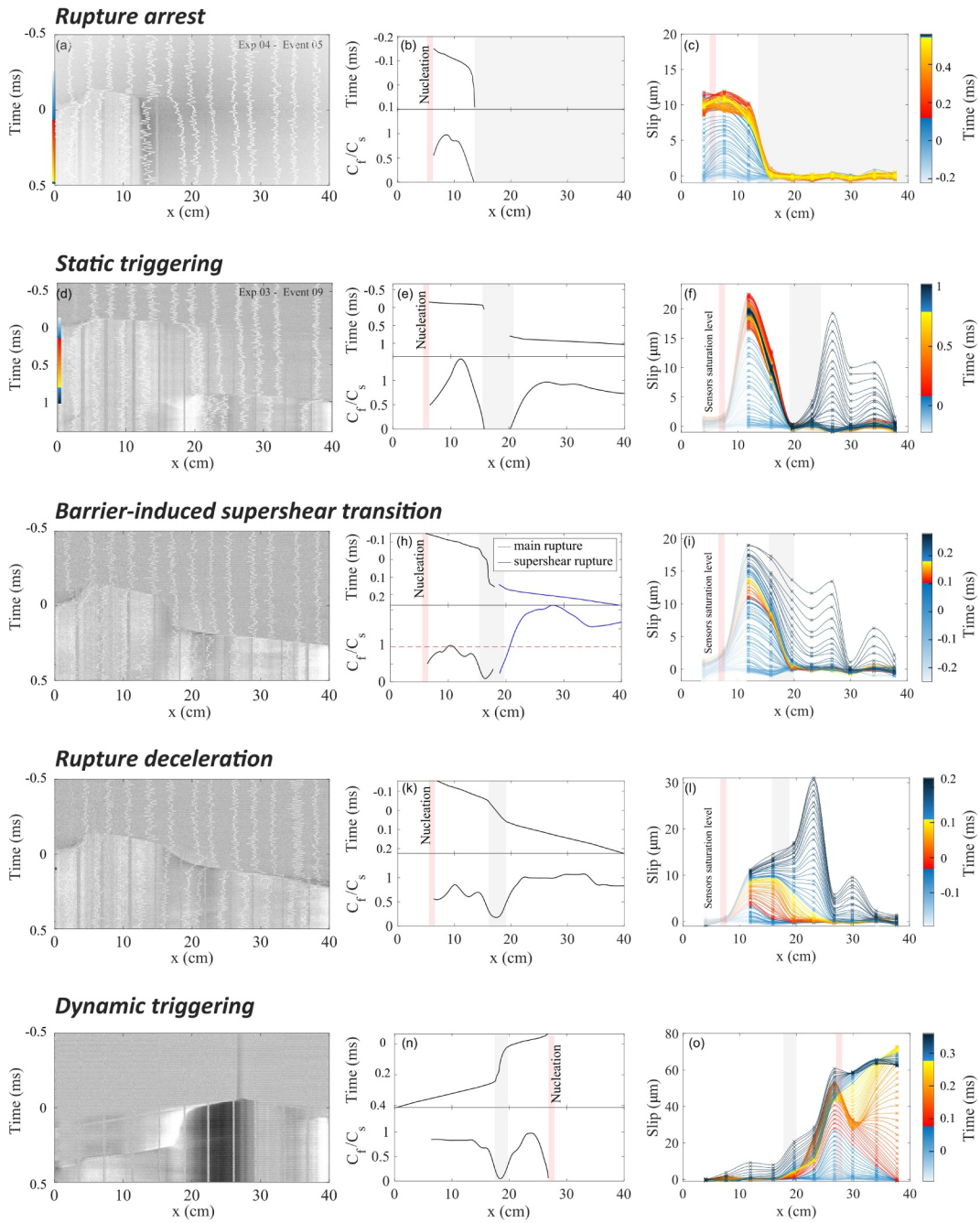

Figure 3. Collection of all representative rupture styles interacting with a stress barrier. (a, d, g, j, m) videogram of the selected rupture, with synchronized shear stress measurements (in white) obtained through the thirteen strain gauge rosettes. Colorbar on the left indicates the time interval selected for subplots (c, f, i, l, o). (b, e, h, k, n) rupture front evolution, obtained through manual picking from the videogram (on the top), and rupture propagation velocity (on the bottom). The red-shaded region indicates the rupture nucleation location, while the gray area indicates a region of either arrest (b) or deceleration (e, h, k, n). (c, f, i, l, o) Spatiotemporal slip distribution during each event. The curves are plotted with a time interval of 5 μs. Note that a different colormap (orange) indicates the period during rupture deceleration. A shaded area indicates cases in which the displacement sensors reached saturation, making their measurements unreliable (x = 3–10 cm for f, i, l, o).

4. Discussion

Our results demonstrate that stress heterogeneity along the fault can exert a strong influence on the dynamics of a propagating rupture (Figure 3). The nature of this interaction depends primarily on the strength of the stress

21699356, 2026, 2, Downloaded from https://agupubs.onlinelibrary.wiley.com/doi/10.1029/2025JB032879 by Charles University T.G., Wiley Online Library on [19/02/2026]. See the Terms and Conditions (https://onlinelibrary.wiley.com/terms-and-conditions) on Wiley Online Library for rules of use; OA articles are governed by the applicable Creative Commons License

barrier. As expected, a sufficiently strong barrier is capable of fully arresting the rupture, whereas a weaker barrier may only reduce its propagation velocity. However, our experiments also revealed several exceptions to this simple picture, indicating that rupture–barrier interactions are not always straightforward. In the following sections, we analyze the physical processes underlying the different interaction mechanisms, presenting them in order from the strongest to the weakest stress barriers.

4.1. Rupture Arrest

When a stress barrier is sufficiently strong, as at the beginning of our experiments, it is likely to arrest the rupture. This behavior can be described using Linear Elastic Fracture Mechanics, where the frictional rupture is modeled as a mode II crack. The propagation of a frictional rupture is controlled by the energy balance at its crack tip. As long as the static energy release rate G_0 (i.e., the energy feeding the rupture propagation) is equal to or larger than the fracture energy G_c (i.e., energy opposing rupture propagation), the rupture will propagate (Freund, 1998). On the contrary, the rupture will arrest if $G_0 < G_c$. The latter case can occur either for a local decrease of G_0 or for a local increase of G_c. Comparing the energy release rate of a rupture to the fault fracture energy allows the prediction of the rupture length (Bayart et al., 2016; Fryer et al., 2024; Kammer et al., 2015; Ke et al., 2018). The static energy release rate is computed as

$$G_0 = \frac{K_{\mathrm{II}}^2\left(1-\nu^2\right)}{E}, \tag{1}$$

with K_{II} the stress intensity factor for a mode II crack, and E and ν the elastic properties of the bulk material. For an edge crack, that is, a rupture reaching the boundary of the sample, with non-uniform stress drop $\Delta\tau$ (Tada et al., 1973):

$$K_{\mathrm{II}}(l) = \frac{2}{\pi l}\int_0^l \Delta\tau(s)\frac{F(s/l)}{\sqrt{1-\left(\frac{s}{l}\right)^2}}ds, \tag{2}$$

with weight function $F(s/l) = 1 + 0.3\left(1 - \left(\frac{s}{l}\right)^{\frac{5}{4}}\right)$. For a seed crack, that is, a rupture contained within the sample and far from its boundaries, it takes the form:

$$K_{\mathrm{II}}(x_{nuc}+l) = \frac{1}{\sqrt{\pi l}}\int_{-l}^{l}\Delta\tau(x_{nuc}+s)\sqrt{\frac{l\pm s}{l\mp s}}ds, \tag{3}$$

where x_{nuc} is the nucleation location. The stress drop along the fault was calculated as $\Delta\tau(x) = \tau_0(x) - \tau_{\mathrm{res}}(x)$, with τ_0 the background stress and τ_{res} the residual stress. The spatial distribution of fracture energy was computed exploiting its relation to normal stress (Bayart et al., 2016).

The following rupture arrest criterion was used: when $G_0/G_c < 1$ the rupture is expected to arrest (Figure 4). For all partial events, the arrest criterion fully predicted the measured arrest location, which occurred between $x = 8$ and 20 cm (Figure 4d). This is concurrent with the negative local stress drop, highlighting the presence of a stress barrier. Similarly, this criterion predicted no arrest for all complete ruptures (Figure 4d). The way the G_0/G_c ratio affects rupture propagation will be detailed later.

Despite the overall good agreement for most events, a few exceptions arise. In three cases, the criterion predicted arrest for ruptures that ultimately propagated across the entire fault. Notably, each of these ruptures did exhibit a temporary halt at the predicted arrest location (indicated by shaded markers in Figure 4), but this triggered an interaction mechanism (static triggering or barrier-induced supershear transition) that is not included in the model, and that led to further rupture propagation. Conversely, in another static-triggering case (shaded blue marker in Figure 4), the criterion predicted no arrest. Nonetheless, the rupture briefly halted before propagating across the entire fault. The physics underlying these additional interaction mechanisms will be examined in the following sections.

21699356, 2026, 2, Downloaded from https://agupubs.onlinelibrary.wiley.com/doi/10.1029/2025JB032879 by Charles University T.G., Wiley Online Library on [19/02/2026]. See the Terms and Conditions (https://onlinelibrary.wiley.com/terms-and-conditions) on Wiley Online Library for rules of use; OA articles are governed by the applicable Creative Commons License

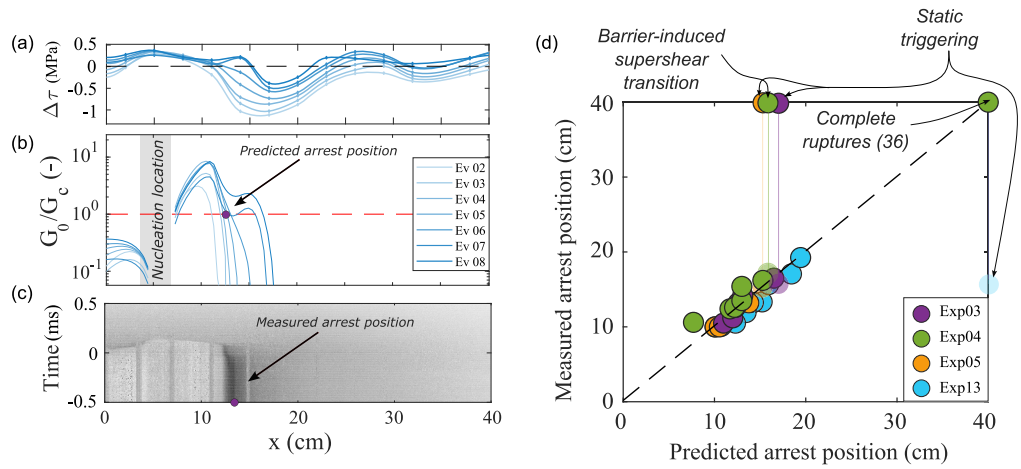

Figure 4. Rupture arrest prediction through linear elastic fracture mechanics. Detailed procedure shown for Experiment 03. (a) Non-uniform stress drop distribution for partial ruptures (Ev 02–08). (b) $\frac{G_0}{G_c}$ distribution. The red dotted line indicates the arrest criterion for $\frac{G_0}{G_c} < 1$. Complete rupture profiles are shown in Section 4.4. (c) Videogram of event 04. Purple dot marks the measured arrest; the same dot marks the predicted arrest in (b). (d) Predicted versus measured rupture arrest position for all ruptures (Exp 03,04,05,13). Partial ruptures align along the 1:1 slope, indicating good prediction, while for complete ruptures, no arrest is predicted. Shaded markers denote the location where ruptures temporarily halted before continuing to propagate further (three cases of static triggering and one case of barrier-induced supershear transition).

4.2. Static Triggering

Stress heterogeneity can also promote static triggering. This occurs when the stress change induced by a rupture increases the stress in neighboring regions of the fault, inducing rupture nucleation. In our data set, we observed this phenomenon three times. In the selected example, a rupture occurred on the left portion of the fault, arresting at $x = 16$ cm. After 0.9 ms, during which no slip occurred (Figure 3), a new rupture nucleated at $x = 25$ cm, rupturing the rest of the fault (Figure 5a). The arrest of the rupture caused a significant shear stress increase ahead of the arrest location. This increase is larger in the vicinity ($\sim$0.2 MPa) and lower, but still significant, further away ($\sim$0.1 MPa) (Figure 5b).

The triggered nucleation can be interpreted using the rate and state simple patch model (Dieterich, 1992), which has been applied to describe rupture jumps across geometrical discontinuities (Kroll et al., 2023; Michel et al., 2025). This model accounts for *remote stressing* caused by slip in an adjacent fault region. If the induced stress increase is sufficiently large, nucleation occurs immediately. For smaller but still significant stress perturbations, the nucleation is delayed by a time t_i until the local shear stress reaches its steady-state value.

The model relies on the empirical slip-rate and state-dependent friction law:

$$\tau = \sigma\left(\mu_0 + a\ln\left(\frac{V}{V_*}\right) + b\ln\left(\frac{V_*\theta}{D_c}\right)\right), \tag{4}$$

where μ_0 is the steady-state friction coefficient at a reference slip rate V_*, a and b are the direct and evolution effect constitutive parameters, respectively, θ is the state variable, and D_c is the characteristic distance for state evolution. Note that Equation 4 is a simplified formulation that does not account for dependence on temperature and normal stress on the friction coefficient (Barbot, 2025). An evolution law accompanies Equation 4 (for instance, the aging law $\dot{\theta} = 1 - \frac{\theta V}{D_c}$).

For a rapid stress change, the slip rate induced on the neighboring fault region is (Kroll et al., 2023):

$$V = V_0 \exp\left(\frac{1}{a\sigma_{n,0}}\left(\Delta\tau - \frac{\tau_0}{\sigma_{n,0}}\Delta\sigma_n\right)\right), \tag{5}$$

21699356, 2026, 2, Downloaded from https://agupubs.onlinelibrary.wiley.com/doi/10.1029/2025JB032879 by Charles University T.G., Wiley Online Library on [19/02/2026]. See the Terms and Conditions (https://onlinelibrary.wiley.com/terms-and-conditions) on Wiley Online Library for rules of use; OA articles are governed by the applicable Creative Commons License

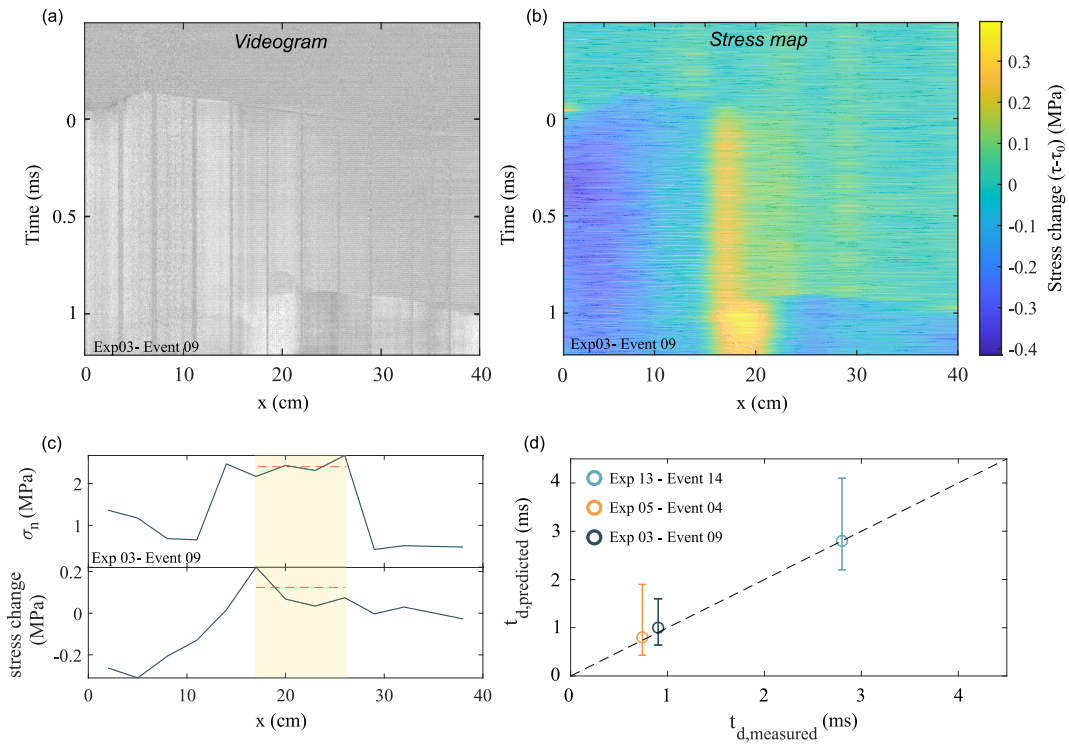

Figure 5. (a) Videogram of one representative example of static triggering (Experiment 03–Event 09). (b) Shear stress change map for the event in (a), obtained by spatially interpolating stress measurements from strain gauges. (c) Initial normal stress distribution (top) and shear stress change before triggering (bottom). The yellow shaded area indicates the area interested by stress change due to the original event. The dashed red line indicates the average value used in Equation 5. (d) Comparison between the expected delay time t_i and the measured delay time t_d for the three observed cases.

where $\Delta\tau$ and $\Delta\sigma$ are the change in shear and normal stress induced by the causative rupture, $\tau_0, \sigma_{n,0}$ the initial shear and normal stress values, and V_0 the initial slip rate.

A time to instability can be computed in the case of null driving stress $\left(\dot{\tau} = 0\right)$ as (Dieterich, 1992):

$$t_i = \frac{a}{H}\left(\frac{1}{V} - \frac{1}{V_{EQ}}\right), \tag{6}$$

where V_{EQ} is the characteristic slip rate during dynamic propagation, and $H = \frac{b}{D_c} - \frac{k}{\sigma}$, with k the stiffness of the patch.

In the studied case, rate and state parameters characteristic of PMMA were used (Cochard et al., 2003): $a = 0.12$, $b = 0.024$, and $D_c = 1e{-}6$ m. V_{EQ} was chosen to be 0.5 m/s as measured in our events during dynamic rupture propagation, and V_0 was set as 10^{-5} m/s. The local stiffness was computed as (Dieterich, 1992) $k = \frac{\Delta\tau}{\delta} \simeq 20$ GPa/m.

Given that, for all three cases, no change in normal stress induced by the original event was observed, the variables to be introduced in Equation 5 reduce to $\sigma_{n,0}$, and $\Delta\tau$. These values were selected by computing an average of their spatial distribution in the region adjacent to the causative event arrest location (Figure 5c, yellow area). This selection allowed the comparison between the expected time to instability (t_i) and the measured one (t_d) (Figure 5d). The strong agreement between the two quantities indicates that the rate and state simple patch model can explain the static triggering mechanism observed in our experiments.

21699356, 2026, 2, Downloaded from https://agupubs.onlinelibrary.wiley.com/doi/10.1029/2025JB032879 by Charles University T.G., Wiley Online Library on [19/02/2026]. See the Terms and Conditions (https://onlinelibrary.wiley.com/terms-and-conditions) on Wiley Online Library for rules of use; OA articles are governed by the applicable Creative Commons License

4.3. Barrier-Induced Supershear Transition

An interaction mechanism largely investigated through analytical and numerical models (Dunham, 2007; Dunham et al., 2003; Lapusta & Liu, 2009; Liu & Lapusta, 2008; Weng et al., 2015), but experimentally observed here for the first time, is the barrier-induced supershear transition. It is known that propagating ruptures can spontaneously transition to supershear velocities (i.e., $C_f > C_s$) if the initial stress is high enough. A key quantity used as a transition criterion is the strength excess ratio $S = \frac{\tau_s - \tau_0}{\tau_0 - \tau_d}$, with τ_s, the static strength, τ_d the dynamic strength, and τ_0 the background shear stress. When $S < S_c = 1.77$ for a distance greater than a given transition length L, a daughter rupture will nucleate and propagate at $C_f > C_s$ (Andrews, 1976; Burridge, 1973). This has been largely observed and studied experimentally (Dong et al., 2023; Kammer et al., 2018; Passelègue et al., 2013; Rubino et al., 2020; Tal et al., 2022; Xia et al., 2004).

However, the presence of stress heterogeneity can also induce a supershear transition through different mechanisms (Dunham, 2007; Dunham et al., 2003; Liu & Lapusta, 2008; Weng et al., 2015). Our observed example exhibits a rupture that nucleated at $x = 6$ cm and propagated bilaterally (Figure 6). It significantly decelerated at $x = 15$ cm, reaching a velocity of $C_f \simeq 0.2C_s$ (Figures 3h and 6). At $x = 19$ cm, a new rupture front nucleated, accelerated, and reached supershear velocity $\left(C_f \simeq 0.9C_p\right)$ after a propagation distance of 3 cm. Similarly to Weng et al. (2015), the dynamic S ratio was computed for several locations along the fault as $S(t) = \frac{\tau_s - \tau(t)}{\tau(t) - \tau_d}$ (Figure 6c).

The $S(t)$ ratio for one selected location before the stress barrier ($x = 13$ cm, indicated by light blue curve in Figure 6c) started from an initial low value (0.8). It remained stable until the drop to zero concurrent with the passage of the rupture ($\tau(t) = \tau_s$), followed by a sudden increase (for $\tau(t) = \tau_d$).

Inside the barrier ($x = 20$ cm, indicated by red curves in Figure 6c), $S(t)$ started from a higher value of ~2, remained constant for a time interval of ~0.2 ms, then gradually decreased over time until dropping to zero concurrent with the passage of the rupture tip. Once the rupture passed by, $S(t)$ promptly increased as expected.

Concerning the location past the barrier ($x = 23$ cm, indicated by dark blue curve in Figure 6c), $S(t)$ started from an already low value of ~0.5. It remained constant for a time interval of ~0.2 ms, then further decreased over time until dropping to zero concurrent with the passage of the rupture tip, before suddenly increasing.

The gradual decrease of $S(t)$ inside the barrier (red curves) and immediately outside (dark blue curves) is controlled by the local increase of stress caused by the initially halted rupture. As in the previous example of static triggering, when a rupture arrests, it generates a stress increase ahead of the arrest location, thus a decrease in $S(t)$, which facilitates the emergence of a new rupture front accelerating to supershear velocities.

In our example, the initial S ratio (S_0) was already low outside of the barrier, with values between 0.07 and 0.2 (from $x = 21$ cm until the end of the fault, Figure 6b). For such a low S_0, one might expect the rupture to transition spontaneously to supershear regardless of the presence of the barrier. However, this is not the case, as the initial shear stress is also very low, resulting in a quite large transition distance (Liu & Lapusta, 2008). Computing the expected transition length as $L = f_s \cdot L_c$, with $f_s = 9.8(Sc - S_0)^{-3}$, and $L_c = \frac{4}{\pi}\frac{\mu}{(1-\nu)}\frac{G_c}{(\tau_0 - \tau_r)}$ (Andrews, 1976; Passelègue et al., 2013), led to a $L \simeq 15$ cm. This transition length is much larger than observed in our example, where the rupture front accelerates to supershear velocity over a distance of only 3 cm. Surely, the low S_0 helped sustain such a high propagation velocity until the end of the fault.

This experimental observation corroborates previous numerical studies, suggesting that a stress barrier can induce supershear transition (Weng et al., 2015). This behavior is governed by the local, gradual decrease of the $S(t)$ ratio over time, driven by the increase in shear stress resulting from the initial rupture arrest.

4.4. Rupture Deceleration

An additional effect of stress heterogeneity interacting with a propagating rupture can result in a simple deceleration. As described in Section 4.1, considering LEFM, the propagation of a frictional rupture is controlled by the energy balance at its tip. This energy balance can then be corrected by the dynamic nature of the propagation phenomenon as $G = G_0 \cdot g\left(C_f\right)$, where $g\left(C_f\right)$ is a universal velocity function, which approaches 1 for slow ruptures and 0 for fast ruptures (Freund, 1998). From this, a direct relation emerges between the rupture velocity

21699356, 2026, 2, Downloaded from https://agupubs.onlinelibrary.wiley.com/doi/10.1029/2025JB032879 by Charles University T.G., Wiley Online Library on [19/02/2026]. See the Terms and Conditions (https://onlinelibrary.wiley.com/terms-and-conditions) on Wiley Online Library for rules of use; OA articles are governed by the applicable Creative Commons License

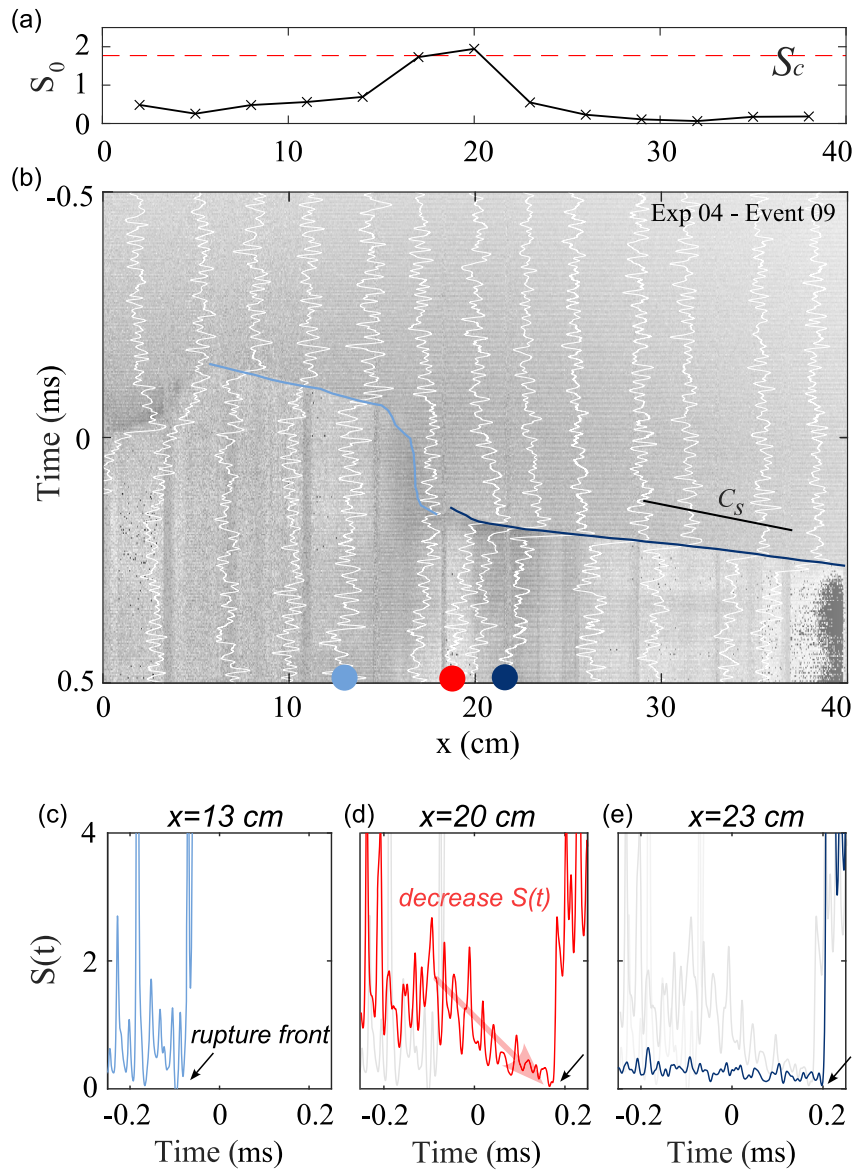

Figure 6. Representative example of barrier-induced supershear transition. (a) Initial S ratio computed along the default. The red dotted line indicates the S_c value. (b) Videogram of the selected event, with synchronized shear stress measurements (in white). Light and dark blue curves indicate the rupture front of the subshear and supershear propagation phases respectively. Markers indicate the location at which $S(t)$ was computed. (c–e) Temporal evolution of $S(t)$ for the three selected locations around and inside the stress barrier.

and the energy ratio, $C_f = f\left(\frac{G_0}{G_c}\right)$, suggesting that any significant change in the energy budget will result in a correspondingly considerable effect on C_f.

Similarly to Section 4.1, the static energy release rate G_0 was computed for all complete ruptures, considering a bilateral crack propagation (following Equation 3, Figure 7a). Around the nucleation location ($x \approx 6$ cm), the fault manifested an overall high G_0/G_c ratio of ~5 (Figure 7b). For increasing crack lengths, the G_0/G_c ratio gradually decreased until dropping, depending on the single event, between 1.1 and 1.8 at $x \sim 20$ cm. For larger crack lengths, the G_0/G_c ratio gradually increased, reaching considerable values (~30) toward the edge of the fault.

21699356, 2026, 2, Downloaded from https://agupubs.onlinelibrary.wiley.com/doi/10.1029/2025JB032879 by Charles University T.G., Wiley Online Library on [19/02/2026]. See the Terms and Conditions (https://onlinelibrary.wiley.com/terms-and-conditions) on Wiley Online Library for rules of use; OA articles are governed by the applicable Creative Commons License

As the G_0/G_c distribution along the fault is expected to control $C_f(x)$, it can be used to predict the propagation velocity profile. In the specific selected sequence, two versions of the universal velocity function were used. The first version is the commonly used approximation $g(C_f) \approx 1 - C_f/C_r$ (Freund, 1998). The second version is the exact function $g(C_f) = A_{II}(C_f) \cdot k(C_f)^2$ (chapter 6, Freund (1998)), where $A_{II}(C_f) = \frac{C_f^2 \alpha_s}{(1-\nu)C_s^2 D}$ is the universal function of rupture velocity for mode II ruptures, with quantities α_s and D depending on C_f, and $k(C_f) = \frac{1 - C_f/C_s}{\sqrt{1 - C_f/C_p}}$ is the universal function of rupture speed for elastic crack growth. Using the approximated function, the obtained rupture profile strongly overestimates the change in velocity due to the G_0/G_c reduction (blue curves in Figures 7c–7i). However, using the exact universal function, the retrieved velocity profile, thus the rupture front, matches the observed one to a satisfactory extent (Figures 7c–7i, red curves). Indeed, when comparing the two versions of the velocity function, a clear discrepancy emerges (Figure 7j), as previously pointed out (Svetlizky et al., 2017). Moreover, note that this solution is derived for an elastic crack growth at a constant speed. This might not perfectly reflect the case presented here, where a quite abrupt deceleration occurs. Interestingly, despite the overall match between the predicted and observed rupture fronts, the largest discrepancy occurs for Event 10, which experienced the largest abrupt deceleration.

4.5. Dynamic Triggering

Another possible interaction mechanism observed in these laboratory sequences is dynamic triggering. It occurs when rupture nucleation is triggered by the passage of a seismic wave emitted by previous ruptures.

In the observed event (Figure 8), a rupture nucleated at $x = 28$ cm and propagated bilaterally. The leftward rupture tip soon encountered the barrier and experienced significant deceleration, reaching a propagation velocity of $\sim 0.1 C_s$. On the other side, the rightward rupture tip reached the fault edge, generating a fault interface Rayleigh wave (FIRW in Ding et al. (2024), also observed by Latour et al. (2024)). Such a Rayleigh wave propagated toward the opposite fault edge and, upon reaching the already slowly propagating rupture front, triggered its sudden re-acceleration. At that point, the rupture propagated at a high velocity $(C_f \sim C_s)$, and after ~7 cm, it transitioned to supershear velocity and continued at that speed to the end of the fault.

The case presented exemplifies how effective dynamic triggering can be in 'advancing the clock' of the second rupture propagation phase. In this specific case, the rupture would have passed through the barrier even without triggering, but over a significantly longer time interval. Dynamic triggering, however, pushed the rupture front through the barrier and anticipated its propagation.

4.6. Barrier Strength Controls Interaction Mechanisms

A propagating rupture can interact with a stress barrier in several ways, as demonstrated in the previous sections. However, the strength of this barrier determines which interaction mechanism will occur. One way to quantify the effect of the barrier on the rupture is to consider the induced time delay, that is, the time interval by which the rupture is slowed down during its propagation. This time delay can be considerable (close to the recurrence time T_R) for arrested ruptures, or minimal (close to the seismic wave travel time t_r), for example, for dynamic triggering or decelerated ruptures.

For all studied events, the time delay (t_d) was measured as the difference between the time at which the rupture reached position $x = 20$ cm (past the barrier), where all ruptures had resumed dynamic propagation, and the time at which the S-wave radiated by the strong deceleration reached the same position (Figure 9, inset). For fast ruptures propagating at $C_f \sim C_s$, this definition predicts $t_d = 0$. The measured t_d spanned a broad range of values, from 0.05 to 2.9 ms (up to ~50 times larger than the S wave propagation time).

Concurrently, a proxy for the strength of the barrier was quantified based on the local stress conditions as $B = (\tau_0^{barr} - \tau_r^{barr})/\tau_0^{barr}$, where τ_0^{barr} denotes the background stress and τ_r^{barr} the residual stress, both at the barrier location ($x = 17$ cm). Negative B values indicate a condition where the patch is locked $(\tau_0^{barr} - \tau_r^{barr} < 0)$ and the driving stress is not high enough to overcome the residual strength. Under such conditions, which correspond to the highest barrier strength, ruptures are expected to arrest. We refer to this as the *arresting barrier* condition. On the contrary, when B is positive $((\tau_0^{barr} - \tau_r^{barr}) > 0)$, the driving stress is high enough to allow

21699356, 2026, 2, Downloaded from https://agupubs.onlinelibrary.wiley.com/doi/10.1029/2025JB032879 by Charles University T.G., Wiley Online Library on [19/02/2026]. See the Terms and Conditions (https://onlinelibrary.wiley.com/terms-and-conditions) on Wiley Online Library for rules of use; OA articles are governed by the applicable Creative Commons License

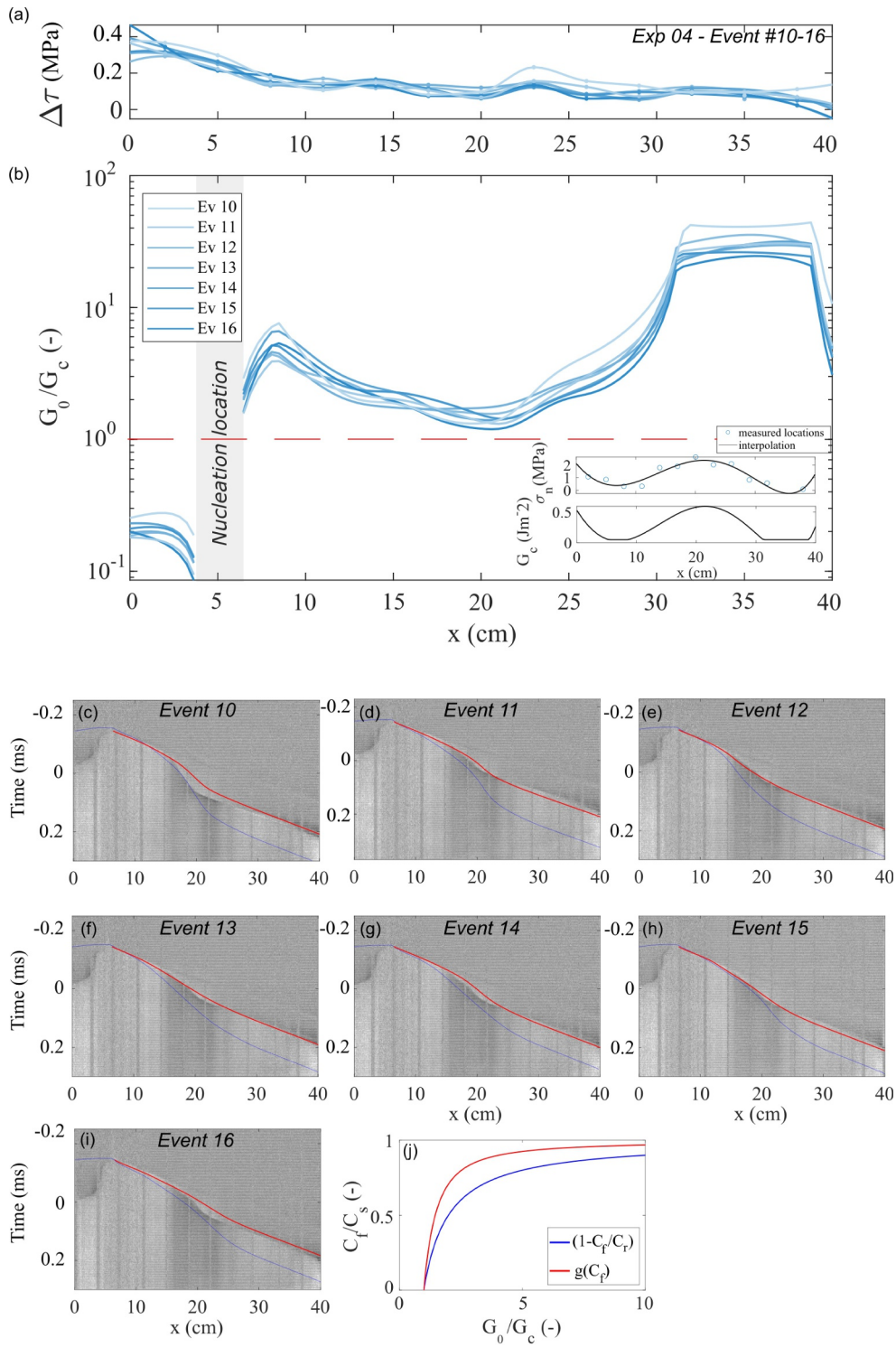

Figure 7. Rupture front prediction through LEFM for Experiment 04. (a) Non-uniform stress drop distribution for all studied partial ruptures (Ev 10–16). (b) $\frac{G_0}{G_c}$ distribution for all ruptures. The red dotted line indicates the arrest criterion for $\frac{G_0}{G_c} < 1$. The inset shows the normal stress distribution and the assumed fracture energy profile. (c–i) Videograms of Ev 10–16 with rupture front prediction using the approximated velocity function (in blue), and its exact solution (in red). (j) Approximation and exact solution for the velocity function $g(C_f)$ as a function of rupture speed and energy ratio.

21699356, 2026, 2, Downloaded from https://agupubs.onlinelibrary.wiley.com/doi/10.1029/2025JB032879 by Charles University T.G., Wiley Online Library on [19/02/2026]. See the Terms and Conditions (https://onlinelibrary.wiley.com/terms-and-conditions) on Wiley Online Library for rules of use; OA articles are governed by the applicable Creative Commons License

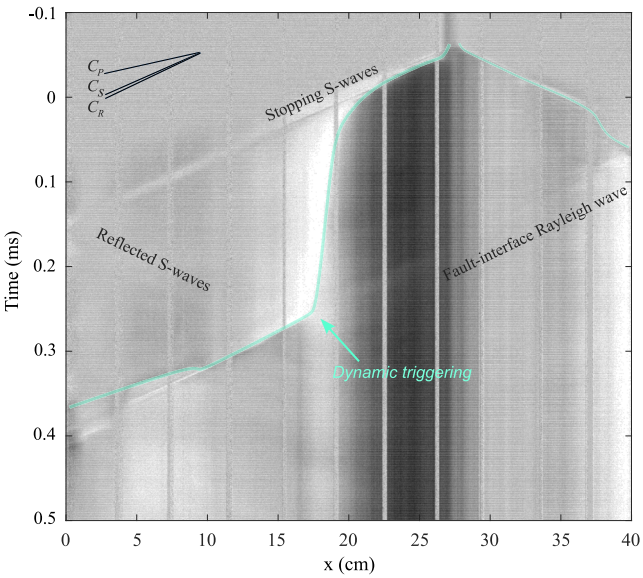

Figure 8. Videogram of the selected example of dynamic triggering. Labels indicate the generated (and/or reflected) seismic waves. The green curve highlights the rupture front.

rupture propagation. The barrier strength becomes smaller as B increases. We refer to this as the *decelerating barrier* condition.

Comparing these quantities across all the studied events reveals a distinct range of time delays (Figure 9). As expected, all partial ruptures occur within the arresting barrier domain, with $t_d = T_R$. Most of the remaining ruptures fall into the B-positive domain, where rupture propagation is not hindered (i.e., decelerating barrier condition). In this region, the time delays collapse along a well-defined curve, corresponding to the deceleration of the propagating rupture. As previously described, this is due to the reduction of the available energy relative to the local fracture energy (decrease of G_0/G_c). The observed time delays range between 0.05 and 1.7 ms, for B values between 0 and 0.19.

Other data points emerge, however, which do not collapse either on the arrested rupture domain or the 'deceleration curve'. One group corresponds to the static-triggered cases (diamond markers in Figure 9). This occurs for B values negative in two cases (−0.8, −0.1) and positive in one (0.1), leading to time delays respectively of 0.75, 0.9, and 2.8 ms. A second group corresponds to the barrier-induced supershear cases (triangle markers in Figure 9). This occurs for B values of −0.11 and −0.01, with both time delays of 0.2 ms. The last group comprises the single observation of dynamic triggering (square marker in Figure 9). This occurs for a B value of 0.02, leading to a time delay of 0.25 ms.

An arresting stress barrier along the fault will arrest a propagating rupture, while a decelerating stress barrier will alter its propagation, locally reducing its velocity. Interestingly, certain interaction mechanisms may diverge from the typically observed framework. Static triggering, for example, can promote rupture propagation even under initial conditions that would normally act as an arresting barrier. More interestingly, the critical case of barrier-induced supershear transition, where not only is the rupture triggered under conditions in which it is not expected, but it also propagates at velocities much higher than otherwise expected. A final example is provided by dynamic triggering. Although this occurs under decelerating barrier conditions, where rupture propagation might indeed be expected, dynamic triggering significantly advances the timing of rupture re-acceleration, causing it to occur well before the time expected by the LEFM deceleration curve. Note that the B parameter is not intended as a predictive tool, but only as a descriptive one. When considering initial stress conditions only, it highlights that some interaction mechanisms (static triggering, barrier-induced supershear transition, and dynamic triggering) can promote rupture histories that are less predictable than others (rupture arrest or smooth propagation).

4.7. Long-Term Evolution of Stress Barrier

It is interesting to observe not only how the single events interact with a stress barrier, but also how such a stress barrier evolves in time, as it is being broken by consecutive events. In our experiments, the first rupture event encounters the strongest stress barrier, that is, negative potential stress drop (Figure 2e.). Its strength gradually diminishes as partial ruptures recurrently stop at the barrier location. As discussed earlier, the rupture generates a stress increase ahead of the arrest location (increase of τ_0^{arr}), modifying the stress distribution, thus the barrier strength for the coming rupture (increase of B, Figure 9, Figure S2 in Supporting Information S1). After a significant number of partial ruptures, which depends on the initial stress distribution (between 5 and 9 events), B reaches a 0 value (Figure 9, Figure S2 in Supporting Information S1). The barrier transitions from arresting ($B < 0$) to decelerating ($B > 0$). Under such conditions, it is easier for a rupture to propagate past the barrier along the entire fault. In our experiments, the first complete ruptures (1–2) were strongly affected by the presence of the barrier, showing significant time delays and positive B values. Despite still being affected by the barrier, the following ruptures manifested shorter time delays concurrently with a higher B. The latter, in fact, reaches a plateau ($B \sim 0.08 - 1.8$), inducing a similar time delay to the propagating ruptures (for similar nucleation conditions). The value of such a plateau depends on the overall stress distribution and is not modified by the

21699356, 2026, 2, Downloaded from https://agupubs.onlinelibrary.wiley.com/doi/10.1029/2025JB032879 by Charles University T.G., Wiley Online Library on [19/02/2026]. See the Terms and Conditions (https://onlinelibrary.wiley.com/terms-and-conditions) on Wiley Online Library for rules of use; OA articles are governed by the applicable Creative Commons License

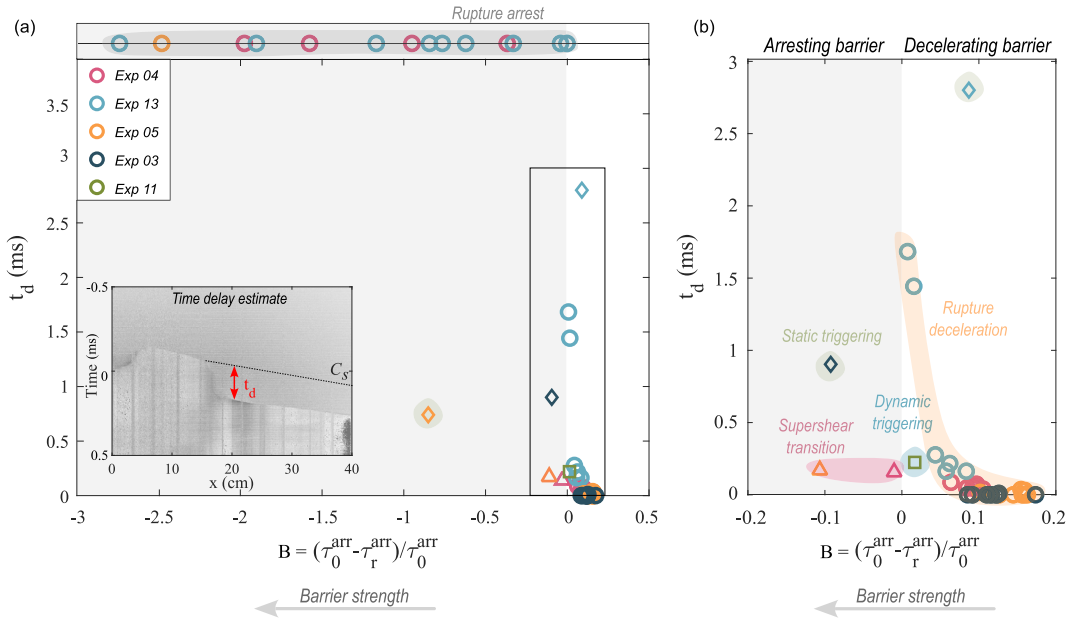

Figure 9. Time delay (t_d) distribution as a function of B value $\left(B = \frac{(\tau_0^{barr} - \tau_r^{barr})}{\tau_0^{barr}}\right)$ (a). Marker color indicates the corresponding experiment, and marker shape denotes the interaction mechanism: circles represent classical LEFM behavior (rupture arrest or deceleration), diamonds indicate static triggering, triangles indicate barrier-induced supershear transition, and squares indicate dynamic triggering. Arrested ruptures, which are not characterized by any t_d, are shown aligned above the main plot, and all fall in the $B < 0$ domain. The remaining events fall into the $B > 0$ domain, with a few exceptions, and their t_d values cover a range between 0.1 and 2.8 ms. The inset illustrates the procedure used to estimate the time delay. (b) Zoom of panel (a).

occurrence of additional complete ruptures. At this point, the stress heterogeneity is incorporated into the along-fault stress distribution and becomes a weak permanent decelerating barrier.

This observation highlights the long-term temporal evolution of a stress barrier for consecutive ruptures. The value of B (inversely proportional to the barrier strength), which is, at the beginning of the experiments, at its lowest (~ -7), increases significantly with the occurrence of partial ruptures. Once complete ruptures start to occur, B soon reaches a plateau, indicating that the barrier has become permanent. However, this is valid under these particular experimental conditions. Note that the fault length to rupture nucleation length ratio is ~ 15, relatively low to induce complex seismic sequences, which are favored by larger ratios (Lapusta & Liu, 2009; Cattania, 2019; Barbot, 2019; S. B. Cebry et al., 2023; Paglialunga, Passelègue, et al., 2025)). The emergence of complex seismic sequences, including partial ruptures between complete ones, could change the way the stress barrier evolves over time. A previous numerical study (Lapusta & Liu, 2009) showed that the presence of a barrier can affect the nucleation location of the ruptures, thus influencing their temporal long-term evolution. S. B. Cebry et al. (2023) showed, with experiments performed on an artificial fault, 1.75 times longer than the one used here, the emergence of complex seismic sequences. In their case, the 'bump' (similar to what we call here a stress barrier) evolves during the seismic sequence, arresting the partial events, and not affecting the complete ones. However, they showed that the bump 'persists over many seismic super cycles'. Other experiments conducted on faults 6.25 times larger also revealed the evolution of stress heterogeneity throughout multiple complex seismic sequences (Paglialunga, Passelègue, et al., 2025). The stress barrier remained constant throughout the entire experiment, although it evolved over the individual seismic cycles, resulting in partial events between complete ones. The dynamics of the complete events were also affected by the stress heterogeneity.

4.8. Interpreting Complex Dynamics of Natural Earthquakes

Natural earthquakes are often characterized by complex rupture dynamics. One example is the 2007 Mw 8.0 Pisco (Peru) earthquake, where two distinct asperities failed, with a time delay of around 60 s (Sladen et al., 2010). A source model of the earthquake, obtained from joint inversion of InSAR and teleseismic data, highlighted two

21699356, 2026, 2, Downloaded from https://agupubs.onlinelibrary.wiley.com/doi/10.1029/2025JB032879 by Charles University T.G., Wiley Online Library on [19/02/2026]. See the Terms and Conditions (https://onlinelibrary.wiley.com/terms-and-conditions) on Wiley Online Library for rules of use; OA articles are governed by the applicable Creative Commons License

main slip patches: one close to the epicenter and a second one occurring ∼60 km away toward the South. The second patch slipped 60 s after the first one. The model resolution does not permit discrimination between a slow rupture propagation between the two slip patches (∼ 1 km/s), or rupture at a usual speed and delayed re-nucleation of the second patch. Despite the uncertainty, the authors find the latter option more reasonable. Indeed, this interpretation bears similarities with our observed example of static triggering. In the experimental event (Exp05-Event 04, Figure S3 in Supporting Information S1), two slip patches occurred on the fault, with a time delay of 1 ms, significantly larger than the dynamic rupture propagation time, leaving the barrier zone unruptured. The time delay is, indeed, controlled by the static stress transfer on the second patch caused by the arrest of the first rupture.

A more recent example of complex rupture is the 2024 Mw 7.5 Noto (Japan) earthquake. In this case, a source inversion combining seismic and geodetic data revealed a dual rupture initiation with a 10 s time delay between the two subevents (Xu et al., 2024). Similarly to the previous example, a first rupture nucleated and propagated for a few kilometers before arresting. After 10 s, a second rupture nucleated around 16 km away from the hypocenter of the first rupture. It propagated bilaterally, finally rupturing the area between the two hypocenters, which had not slipped until that moment. Interestingly, this zone is the one that experienced the largest amount of slip. This indicates that the same area acted as an arresting barrier during the first stage of the rupture, and as an asperity during the second stage, enhancing further slip. Unlike the Pisco earthquake, where the two ruptures are spatially separated with no slip in between, in the Noto earthquake, once the rupture nucleated on the opposite side of the barrier, it propagated backward, rupturing through the barrier and inducing further slip. This behavior could also be described as a case of static triggering. In particular, it bears similarities to event 14 from Experiment 13 (Figure S3 in Supporting Information S1). In our observed event, the second rupture nucleating on the other side of the barrier propagates bilaterally, finally breaking it and allowing slip.

These two examples demonstrate how, despite their simplifying assumptions, laboratory frictional ruptures can be representative of the rupture behavior of natural earthquakes and provide support in interpreting their rupture history.

5. Conclusions

Our experimental study shows that a propagating rupture can interact with a stress barrier in different ways, depending on its strength. In particular, stronger barriers arrest ruptures, while weaker ones cause their deceleration. Surely, these cases are abundantly observed and studied, and are well described by the Linear Elastic Fracture Mechanics theory, considering the frictional rupture as a shear crack. However, although of rarer occurrence compared to the ones just mentioned, other interaction mechanisms were observed in this work, not necessarily described by the same theoretical framework. In particular, cases of static triggering, that is, rupture triggered by static stress increase induced by a previous one, need the introduction of a more complex rate and state model to be described and predicted. Although occurring less frequently (4% of the measured ruptures experienced static triggering), this interaction mechanism can be highly effective, as it can trigger ruptures under unfavorable stress states (i.e., arresting barrier conditions). Similarly, the barrier-induced supershear transition mechanism is also very effective. It is expected to occur only for a critical stress state, with the barrier strength at the boundary between arresting and decelerating. On the contrary, this interaction is far from rupture arrest or deceleration, as it fuels the rupture's transition to supershear velocity over a short distance. A last observed interaction mechanism is dynamic triggering. This is more difficult to predict as it depends not only on the barrier strength, but also on the overall along-fault stress distribution and rupture history. In our experiments, it occurred in a case of decelerating barrier conditions. It can push the propagating rupture through the barrier, advancing its propagation and significantly reducing the barrier-induced time delay.

These observations collectively highlight that the majority of the ruptures respond to stress heterogeneity in an expected way, that is, arresting or decelerating, as described by linear elastic fracture mechanics. In these cases, the rupture history can be predicted if the stress distribution is known. However, despite their rare statistical occurrence, other unexpected mechanisms can take place, which do not respond to the same framework. These more complex ruptures remain, to date, unpredictable.

Moreover, regardless of their nature, most interaction mechanisms featured a time delay in the rupture propagation. This phenomenon shares similarity with the concept of delayed triggering observed in natural earthquakes.

21699356, 2026, 2, Downloaded from https://agupubs.onlinelibrary.wiley.com/doi/10.1029/2025JB032879 by Charles University T.G., Wiley Online Library on [19/02/2026]. See the Terms and Conditions (https://onlinelibrary.wiley.com/terms-and-conditions) on Wiley Online Library for rules of use; OA articles are governed by the applicable Creative Commons License

It is then crucial to consider the role of heterogeneous stress distribution when studying complex rupture dynamics and interpreting earthquake source models.

Conflict of Interest

The authors declare no conflicts of interest relevant to this study.

Data Availability Statement

The data used in this study are publicly available at https://doi.org/10.5281/zenodo.16782075 (Paglialunga, Ampuero, & Passelegue, 2025).

Acknowledgments
F. P. acknowledges support from the SNF PostDoc.Mobility Grant P500PN_222262. F. X. P. acknowledges support from the European Research Council Starting Grant project HOPE 101041966. J. P. A. acknowledges support the French government through the UCAJEDI Investments in the Future project (ANR-15-IDEX-01) managed by the National Research Agency (ANR). F. P. thanks Barnaby Fryer and Corentin Noël for their support in the laboratory and assistance with sample preparation. The authors also thank the two anonymous reviewers, as well as the associated editor and Editor Satoshi Ide, for their constructive comments, which helped improve the manuscript.

References

Andrews, D. J. (1976). Rupture velocity of plane strain shear cracks. *Journal of Geophysical Research*, *81*(32), 5679–5687. https://doi.org/10.1029/JB081i032p05679

Barbot, S. (2019). Slow-slip, slow earthquakes, period-two cycles, full and partial ruptures, and deterministic chaos in a single asperity fault. *Tectonophysics*, *768*, 228171. https://doi.org/10.1016/j.tecto.2019.228171

Barbot, S. (2025). The slip-rate, state-temperature-and normal-stress-dependence of fault friction. *Earthquake Science*, *38*(4), 304–338. https://doi.org/10.1016/j.eqs.2025.03.005

Barras, F., Thøgersen, K., Aharonov, E., & Renard, F. (2023). How do earthquakes stop? Insights from a minimal model of frictional rupture. *Journal of Geophysical Research: Solid Earth*, *128*(8), e2022JB026070. https://doi.org/10.1029/2022jb026070

Bayart, E., Svetlizky, I., & Fineberg, J. (2016). Fracture mechanics determine the lengths of interface ruptures that mediate frictional motion. *Nature Physics*, *12*(2), 166–170. https://doi.org/10.1038/nphys3539

Bayart, E., Svetlizky, I., & Fineberg, J. (2018). Rupture dynamics of heterogeneous frictional interfaces. *Journal of Geophysical Research: Solid Earth*, *123*(5), 3828–3848. https://doi.org/10.1002/2018JB015509

Brodsky, E. E., Karakostas, V., & Kanamori, H. (2000). A new observation of dynamically triggered regional seismicity: Earthquakes in Greece following the August 1999 Izmit, Turkey earthquake. *Geophysical Research Letters*, *27*(17), 2741–2744. https://doi.org/10.1029/2000gl011534

Buijze, L., Guo, Y., Niemeijer, A., Ma, S., & Spiers, C. (2020). Nucleation of stick-slip instability within a large-scale experimental fault: Effects of stress heterogeneities due to loading and gouge layer compaction. *Journal of Geophysical Research: Solid Earth*, *125*(8), e2019JB018429. https://doi.org/10.1029/2019jb018429

Burridge, R. (1973). Admissible speeds for plane-strain self-similar shear cracks with friction but lacking cohesion. *Geophysical Journal of the Royal Astronomical Society*, *35*(4), 439–455. https://doi.org/10.1111/j.1365-246X.1973.tb00608.x

Cattania, C. (2019). Complex earthquake sequences on simple faults. *Geophysical Research Letters*, *46*(17–18), 10–384. https://doi.org/10.1029/2019gl083628

Cebry, S., & McLaskey, G. (2024). Heterogeneous high frequency seismic radiation from complex ruptures. *Seismica*, *3*(2). https://doi.org/10.26443/seismica.v3i2.1351

Cebry, S. B., Ke, C. Y., & McLaskey, G. C. (2022). The role of background stress State in fluid-induced aseismic slip and dynamic rupture on a 3-m laboratory fault. *Journal of Geophysical Research: Solid Earth*, *127*(8), 1–19. https://doi.org/10.1029/2022JB024371

Cebry, S. B., Ke, C.-Y., Shreedharan, S., Marone, C., Kammer, D. S., & McLaskey, G. C. (2022). Creep fronts and complexity in laboratory earthquake sequences illuminate delayed earthquake triggering. *Nature Communications*, *13*(1), 6839. https://doi.org/10.1038/s41467-022-34397-0

Cebry, S. B., Sorhaindo, K., & McLaskey, G. C. (2023). Laboratory earthquake rupture interactions with a high normal stress bump. *Journal of Geophysical Research: Solid Earth*, *128*(11), e2023JB027297. https://doi.org/10.1029/2023jb027297

Cochard, A., Bureau, L., & Baumberger, T. (2003). Stabilization of frictional sliding by normal load modulation. *Journal of Applied Mechanics*, *70*(2), 220–226. https://doi.org/10.1115/1.1546241

Dal Zilio, L., van Dinther, Y., Gerya, T., & Avouac, J. P. (2019). Bimodal seismicity in the Himalaya controlled by fault friction and geometry. *Nature Communications*, *10*, 1–11. https://doi.org/10.1038/s41467-018-07874-8

Das, S., & Aki, K. (1977). Fault plane with barriers: A versatile earthquake model. *Journal of Geophysical Research*, *82*(36), 5658–5670. https://doi.org/10.1029/jb082i036p05658

Das, S., & Kostrov, B. (1983). Breaking of a single asperity: Rupture process and seismic radiation. *Journal of Geophysical Research*, *88*(B5), 4277–4288. https://doi.org/10.1029/jb088ib05p04277

Day, S. M. (1982). Three-dimensional simulation of spontaneous rupture: The effect of nonuniform prestress. *Bulletin of the Seismological Society of America*, *72*(6A), 1881–1902. https://doi.org/10.1785/bssa07206a1881

Dieterich, J. H. (1992). Earthquake nucleation on faults with rate-and state-dependent strength. *Tectonophysics*, *211*(1–4), 115–134. https://doi.org/10.1016/0040-1951(92)90055-b

Ding, X., Xu, S., Fukuyama, E., & Yamashita, F. (2024). Back-propagating rupture: Nature, excitation, and implications. *Journal of Geophysical Research: Solid Earth*, *129*(10), e2024JB029629. https://doi.org/10.1029/2024jb029629

Dong, P., Xia, K., Xu, Y., Elsworth, D., & Ampuero, J.-P. (2023). Laboratory earthquakes decipher control and stability of rupture speeds. *Nature Communications*, *14*(1), 2427. https://doi.org/10.1038/s41467-023-38137-w

Dublanchet, P., Bernard, P., & Favreau, P. (2013). Interactions and triggering in a 3-D rate-and-state asperity model. *Journal of Geophysical Research: Solid Earth*, *118*(5), 2225–2245. https://doi.org/10.1002/jgrb.50187

Dunham, E. M. (2007). Conditions governing the occurrence of supershear ruptures under slip-weakening friction. *Journal of Geophysical Research*, *112*(B7). https://doi.org/10.1029/2006jb004717

Dunham, E. M., Favreau, P., & Carlson, J. M. (2003). A supershear transition. *Science Reports*, *299*(5612), 1557–1559. https://doi.org/10.1126/science.1080650

Freed, A. M. (2005). Earthquake triggering by static, dynamic, and postseismic stress transfer. *Annual Review of Earth and Planetary Sciences*, *33*(1), 335–367. https://doi.org/10.1146/annurev.earth.33.092203.122505

21699356, 2026, 2, Downloaded from https://agupubs.onlinelibrary.wiley.com/doi/10.1029/2025JB032879 by Charles University T.G., Wiley Online Library on [19/02/2026]. See the Terms and Conditions (https://onlinelibrary.wiley.com/terms-and-conditions) on Wiley Online Library for rules of use; OA articles are governed by the applicable Creative Commons License

Freund, L. B. (1998). *Dynamic fracture mechanics*. Cambridge University Press.

Fryer, B., Lebihain, M., Noël, C., Paglialunga, F., & Passelègue, F. (2024). The effect of stress barriers on unconventional-singularity-driven frictional rupture. *Journal of the Mechanics and Physics of Solids*, *193*, 105876. https://doi.org/10.1016/j.jmps.2024.105876

Fukuyama, E., & Madariaga, R. (2000). Dynamic propagation and interaction of a rupture front on a planar fault. *Pure and Applied Geophysics*, *157*(11), 1959–1979. https://doi.org/10.1007/978-3-0348-7695-7_9

Gabrieli, T., & Tal, Y. (2025). Lab earthquakes reveal a wide range of rupture behaviors controlled by fault bends. *Proceedings of the National Academy of Sciences*, *122*(17), e2425471122. https://doi.org/10.1073/pnas.2425471122

Gomberg, J., Bodin, P., & Reasenberg, P. A. (2003). Observing earthquakes triggered in the near field by dynamic deformations. *Bulletin of the Seismological Society of America*, *93*(1), 118–138. https://doi.org/10.1785/0120020075

Gomberg, J., & Johnson, P. (2005). Dynamic triggering of earthquakes. *Nature*, *437*(7060), 830. https://doi.org/10.1038/437830a

Gounon, A., Latour, S., Letort, J., & El Arem, S. (2022). Rupture nucleation on a periodically heterogeneous interface. *Geophysical Research Letters*, *49*(20), e2021GL096816. https://doi.org/10.1029/2021gl096816

Guérin-Marthe, S., Nielsen, S., Bird, R., Giani, S., & Di Toro, G. (2019). Earthquake nucleation size: Evidence of loading rate dependence in laboratory faults. *Journal of Geophysical Research: Solid Earth*, *124*(1), 689–708. https://doi.org/10.1029/2018JB016803

Gvirtzman, S., & Fineberg, J. (2021). Nucleation fronts ignite the interface rupture that initiates frictional motion. *Nature Physics*, *17*(9), 1037–1042. https://doi.org/10.1038/s41567-021-01299-9

Gvirtzman, S., & Fineberg, J. (2023). The initiation of frictional motion—the nucleation dynamics of frictional ruptures. *Journal of Geophysical Research: Solid Earth*, *128*(2), e2022JB025483. https://doi.org/10.1029/2022jb025483

Hardebeck, J. L., Llenos, A. L., Michael, A. J., Page, M. T., Schneider, M., & van der Elst, N. J. (2024). Aftershock forecasting. *Annual Review of Earth and Planetary Sciences*, *52*(1), 61–84. https://doi.org/10.1146/annurev-earth-040522-102129

Hill, D. P., Reasenberg, P., Michael, A., Arabaz, W., Beroza, G., Brumbaugh, D., et al. (1993). Seismicity remotely triggered by the magnitude 7.3 landers, California, earthquake. *Science*, *260*(5114), 1617–1623. https://doi.org/10.1126/science.260.5114.1617

Huang, Y., Ampuero, J.-P., & Kanamori, H. (2014). Slip-weakening models of the 2011 tohoku-oki earthquake and constraints on stress drop and fracture energy. *Pure and Applied Geophysics*, *171*(10), 2555–2568. https://doi.org/10.1007/s00024-013-0718-2

Kammer, D. S., Radiguet, M., Ampuero, J. P., & Molinari, J. F. (2015). Linear elastic fracture mechanics predicts the propagation distance of frictional slip. *Tribology Letters*, *57*(3), 23. https://doi.org/10.1007/s11249-014-0451-8

Kammer, D. S., Svetlizky, I., Cohen, G., & Fineberg, J. (2018). The equation of motion for supershear frictional rupture fronts. *Science Advances*, *4*(7), eaat5622. https://doi.org/10.1126/sciadv.aat5622

Kaneko, Y., Avouac, J. P., & Lapusta, N. (2010). Towards inferring earthquake patterns from geodetic observations of interseismic coupling. *Nature Geoscience*, *3*(5), 363–369. https://doi.org/10.1038/ngeo843

Ke, C. Y., McLaskey, G. C., & Kammer, D. S. (2018). Rupture termination in laboratory-generated earthquakes. *Geophysical Research Letters*, *45*(23), 12784–12792. https://doi.org/10.1029/2018GL080492

Kroll, K. A., Dieterich, J. H., Richards-Dinger, K. B., & Oglesby, D. D. (2023). 3-d simulations of earthquakes rupture jumps: 1. Homogeneous pre-stress conditions. *Geophysical Journal International*, *234*(1), 395–403. https://doi.org/10.1093/gji/ggad048

Lapusta, N., & Liu, Y. (2009). Three-dimensional boundary integral modeling of spontaneous earthquake sequences and aseismic slip. *Journal of Geophysical Research*, *114*(B9). https://doi.org/10.1029/2008jb005934

Lapusta, N., & Rice, J. R. (2003). Nucleation and early seismic propagation of small and large events in a crustal earthquake model. *Journal of Geophysical Research*, *108*(B4), 1–18. https://doi.org/10.1029/2001JB000793

Latour, S., Passelègue, F., Paglialunga, F., Noël, C., & Ampuero, J.-P. (2024). What happens when two ruptures collide? *Geophysical Research Letters*, *51*(20), e2024GL110835. https://doi.org/10.1029/2024gl110835

Latour, S., Schubnel, A., Nielsen, S., Madariaga, R., & Vinciguerra, S. (2013). Characterization of nucleation during laboratory earthquakes. *Geophysical Research Letters*, *40*(19), 5064–5069. https://doi.org/10.1002/grl.50974

Liu, Y., & Lapusta, N. (2008). Transition of mode ii cracks from sub-rayleigh to intersonic speeds in the presence of favorable heterogeneity. *Journal of the Mechanics and Physics of Solids*, *56*(1), 25–50. https://doi.org/10.1016/j.jmps.2007.06.005

Lui, S. K., & Lapusta, N. (2016). Repeating microearthquake sequences interact predominantly through postseismic slip. *Nature Communications*, *7*(1), 13020. https://doi.org/10.1038/ncomms13020

Madariaga, R., & Olsen, K. B. (2001). Criticality of rupture dynamics in 3-d. Microscopic and macroscopic simulation: Towards predictive modelling of the earthquake process (pp. 1981–2001). https://doi.org/10.1007/PL00001071

Michel, S., Scotti, O., Hok, S., Bhat, H. S., Kheirdast, N., Romanet, P., et al. (2025). Probability of earthquake fault jumps from physics based criterion. arXiv preprint arXiv:2501.15948.

Molina-Ormazabal, D., Ampuero, J.-P., & Tassara, A. (2023). Diverse slip behaviour of velocity-weakening fault barriers. *Nature Geoscience*, *16*(12), 1200–1207. https://doi.org/10.1038/s41561-023-01312-1

Morad, D., Gvirtzman, S., Gil, Y., Fineberg, J., & Brodsky, E. (2025). Under what circumstances is the final size of a laboratory earthquake predictable at the onset of the p-wave? *Earth and Planetary Science Letters*, *665*, 119436. https://doi.org/10.1016/j.epsl.2025.119436

Nielsen, S., Taddeucci, J., & Vinciguerra, S. (2010). Experimental observation of stick-slip instability fronts. *Geophysical Journal International*, *180*(2), 697–702. https://doi.org/10.1111/j.1365-246X.2009.04444.x

Noël, C., Twardzik, C., Dublanchet, P., & Passelègue, F. (2025). On the emergence of fault afterslip during laboratory seismic cycles. *Earth and Planetary Science Letters*, *658*, 119288. https://doi.org/10.1016/j.epsl.2025.119288

Paglialunga, F., Ampuero, J. P., & Passelegue, F. (2025). Data repository for: "Stress barriers and their impact on rupture propagation" [Dataset]. *Zenodo*. https://doi.org/10.5281/zenodo.16782075

Paglialunga, F., Passelègue, F., Ampuero, J. P., Latour, S., & Violay, M. (2025). The role of stress distribution in seismic cycle complexity of a long laboratory fault. *Geophysical Research Letters*, *52*(18), e2025GL116440. https://doi.org/10.1029/2025gl116440

Paglialunga, F., Passelegue, F., Latour, S., Gounon, A., & Violay, M. (2023). Influence of viscous lubricant on nucleation and propagation of frictional ruptures. *Journal of Geophysical Research: Solid Earth*, *128*(4), e2022JB026090. https://doi.org/10.1029/2022jb026090

Passelègue, F. X., Schubnel, A., Nielsen, S., Bhat, H. S., & Madariaga, R. (2013). From sub-rayleigh to supershear ruptures during stick-slip experiments on crustal rocks. *Science*, *340*(6137), 1208–1211. https://doi.org/10.1126/science.1235637

Ripperger, J., Ampuero, J.-P., Mai, P., & Giardini, D. (2007). Earthquake source characteristics from dynamic rupture with constrained stochastic fault stress. *Journal of Geophysical Research*, *112*(B4). https://doi.org/10.1029/2006jb004515

Rodriguez Padilla, A. M., Oskin, M. E., Brodsky, E. E., Dascher-Cousineau, K., Herrera, V., & White, S. (2024). The influence of fault geometrical complexity on surface rupture length. *Geophysical Research Letters*, *51*(20), e2024GL109957. https://doi.org/10.1029/2024gl109957

21699356, 2026, 2, Downloaded from https://agupubs.onlinelibrary.wiley.com/doi/10.1029/2025JB032879 by Charles University T.G., Wiley Online Library on [19/02/2026]. See the Terms and Conditions (https://onlinelibrary.wiley.com/terms-and-conditions) on Wiley Online Library for rules of use; OA articles are governed by the applicable Creative Commons License

Romanet, P., Bhat, H. S., Jolivet, R., & Madariaga, R. (2018). Fast and slow slip events emerge due to fault geometrical complexity. *Geophysical Research Letters*, *45*(10), 4809–4819. https://doi.org/10.1029/2018gl077579

Rubino, V., Rosakis, A. J., & Lapusta, N. (2020). Spatiotemporal properties of sub-rayleigh and supershear ruptures inferred from full-field dynamic imaging of laboratory experiments. *Journal of Geophysical Research: Solid Earth*, *125*(2), 1–25. https://doi.org/10.1029/2019JB018922

Schubnel, A., Nielsen, S., Taddeucci, J., Vinciguerra, S., & Rao, S. (2011). Photo-acoustic study of subshear and supershear ruptures in the laboratory. *Earth and Planetary Science Letters*, *308*(3–4), 424–432. https://doi.org/10.1016/j.epsl.2011.06.013

Sheng, S.-Z., Mi, Z.-F., Zhang, X.-J., & Ge, K.-P. (2024). Static stress triggering effect on the surrounding major faults and aftershocks of the 2024 m 7.4 earthquake in Hualien, Taiwan. *Applied Geophysics*, *22*(2), 1–12. https://doi.org/10.1007/s11770-024-1136-1

Sladen, A. A., Tavera, H., Simons, M., Avouac, J.-P., Konca, A., Perfettini, H., et al. (2010). Source model of the 2007 mw 8.0 pisco, Peru earthquake: Implications for seismogenic behavior of subduction megathrusts. *Journal of Geophysical Research*, *115*(B2). https://doi.org/10.1029/2009JB006429

Song, J. Y., & McLaskey, G. C. (2024). Laboratory earthquake ruptures contained by velocity strengthening fault patches. *Journal of Geophysical Research: Solid Earth*, *129*(4). https://doi.org/10.1029/2023jb028509

Svetlizky, I., & Fineberg, J. (2014). Classical shear cracks drive the onset of dry frictional motion. *Nature*, *509*(7499), 205–208. https://doi.org/10.1038/nature13202

Svetlizky, I., Kammer, D., Bayart, E., Cohen, G., & Fineberg, J. (2017). Brittle fracture theory predicts the equation of motion of frictional rupture fronts. *Physical Review Letters*, *118*(12), 125501. https://doi.org/10.1103/PhysRevLett.118.125501

Tada, H., Paris, P. C., & Irwin, G. R. (1973). *The stress analysis of cracks*. Handbook, Del Research Corporation.34.

Tal, Y., Rubino, V., Rosakis, A. J., & Lapusta, N. (2022). Dynamics and near-field surface motions of transitioned supershear laboratory earthquakes in thrust faults. *Journal of Geophysical Research: Solid Earth*, *127*(3), e2021JB023733. https://doi.org/10.1029/2021jb023733

Wang, J.-C., Shieh, C.-F., & Chang, T.-M. (2003). Static stress changes as a triggering mechanism of a shallow earthquake: Case study of the 1999 chi–chi (Taiwan) earthquake. *Physics of the Earth and Planetary Interiors*, *135*(1), 17–25. https://doi.org/10.1016/s0031-9201(02)00175-9

Wang, L., Xu, S., Zhuo, Y., Liu, P., & Ma, S. (2024). Unraveling the roles of fault asperities over earthquake cycles. *Earth and Planetary Science Letters*, *636*, 118711. https://doi.org/10.1016/j.epsl.2024.118711

Weng, H., Huang, J., & Yang, H. (2015). Barrier-induced supershear ruptures on a slip-weakening fault. *Geophysical Research Letters*, *42*(12), 4824–4832. https://doi.org/10.1002/2015gl064281

Xia, K., Rosakis, A. J., & Kanamori, H. (2004). Laboratory earthquakes: The sub-rayleigh-to-supershear rupture transition. *Science*, *303*(5665), 1859–1861. https://doi.org/10.1126/science.1094022

Xu, L., Ji, C., Meng, L., Ampuero, J.-P., Yunjun, Z., Mohanna, S., & Aoki, Y. (2024). Dual-initiation ruptures in the 2024 noto earthquake encircling a fault asperity at a swarm edge. *Science*, *385*(6711), 871–876. https://doi.org/10.1126/science.adp0493

21699356, 2026, 2, Downloaded from https://agupubs.onlinelibrary.wiley.com/doi/10.1029/2025JB032879 by Charles University T.G., Wiley Online Library on [19/02/2026]. See the Terms and Conditions (https://onlinelibrary.wiley.com/terms-and-conditions) on Wiley Online Library for rules of use; OA articles are governed by the applicable Creative Commons License